Three-Dimensional Atom-Probe Tomography: Advances and Applications

David N. Seidman

Department of Materials Science and Engineering, Northwestern University Center for Atom-Probe Tomography, Northwestern University, Evanston, Illinois 60208-3108; email: d-seidman@northwestern.edu

Annu. Rev. Mater. Res. 2007. 37:127–58

First published online as a Review in Advance on April 4, 2007

The *Annual Review of Materials Research* is online at http://matsci.annualreviews.org

This article's doi: 10.1146/annurev.matsci.37.052506.084200

1531-7331/07/0804-0127$20.00

Key Words

field-ion microscopy, time-of-flight mass spectrometry, laser-assisted LEAP^{TM} tomography, α-Al/Al_3Sc heterophase interfaces, Ni-Al-Cr alloys, Ni-Al-Cr-Re alloys, InAs nanowires

Abstract

This review presents the historical temporal evolution of an atom-probe tomograph (APT) from its genesis (1973) from field-ion microscope images of individual tungsten atoms (1955). The capabilities of modern APTs employing either electrical or laser pulsing are discussed. The results of the application of APTs to specific materials science problems are presented for research performed at Northwestern University on the following problems: (*a*) the segregation of Mg at α-Al/Al_3Sc heterophase interfaces, (*b*) phase decomposition in ternary Ni-Al-Cr and quaternary Ni-Al-Cr-Re alloys, and (*c*) 3-D nanoscale composition mapping of an InAs semiconductor nanowire whose growth was catalyzed by gold. These results demonstrate that it is now possible to obtain highly quantitative information from APT that can be compared with modeling, theory, simulations, and/or first-principles calculations.

APT: atom-probe tomography

FIM: field-ion microscope

VLS technique: vapor-liquid-solid technique

Field ionization: ionization of a gas atom in a high electric field by quantum-mechanical tunnelling of its outermost electron

INTRODUCTION

"Nothing tends so much to the advancement of knowledge as the application of a new instrument. The native intellectual powers of men in different times are not so much the causes of the different success of their labours, as the peculiar nature of the means and artificial resources in their possession." This astute observation by Sir Humphry Davy is pertinent to the subject of this review, atom-probe tomography (APT) and its application to problems in materials research. APT has now come of age because commercial atom-probe tomographic instruments that are sophisticated and ergonomic to use are now available to researchers. In this brief review, I first discuss, from an historical point of view, the genesis of atom-probe tomographs (APTs), starting with the invention of the field-ion microscope (FIM), which provided us with the first images of atoms in direct space on October 11, 1955. After discussing the FIM I proceed to review modern APTs, which permit a researcher to reconstruct the positions of atoms in a crystalline specimen in 3-D along with their chemical identities. I then discuss the following selected applications from research performed at Northwestern University that illustrate the unique results obtainable by APT: (*a*) the segregation of Mg atoms at a coherent α-Al/Al_3Sc heterophase interface in a ternary Al-Sc-Mg alloy; (*b*) the kinetic pathways for the nucleation, growth, and coarsening of $Ni_3(Al_{1-x}Cr_x)$ ($L1_2$ structure) γ'-precipitates; (*c*) the kinetic pathways for the nucleation, growth, and coarsening of γ'-precipitates in a quaternary Ni-Al-Cr-Re alloy; and (*d*) the characterization of InAs nanowires that are grown by the vapor-liquid-solid (VLS) technique and that are catalyzed by Au.

INSTRUMENTATION

Field-Ion Microscopy

On October 11, 1955, Müller & Bahadur (Pennsylvania State University) observed individual tungsten (W) atoms on the surface of a sharply pointed W tip by cooling it to 78 K and employing helium as the imaging gas (1). Müller & Bahadur were the first persons to observe individual atoms directly; to do so, they used an FIM, which Müller had invented in 1951 (2, 3). This historic and seminal event occurred long before observations of individual atoms by Z-contrast scanning transmission electron microscopy (STEM), high-resolution electron microscopy (HREM), scanning tunneling microscopy (STM), or atomic-force microscopy (AFM).

An FIM is a lensless point-projection microscope that resolves individual atoms on the surface of a sharply pointed tip at magnifications of greater than 10^6 times. The radius of a tip is <50 nm and is maintained at a positive potential (V_{ex}) with respect to Earth. Atomic-resolution FIM images are achieved by cooling a tip into the range of 20–100 K in a high to ultrahigh vacuum system and placing it at V_{ex} to generate electric fields (**E**-fields) that are between 15 to 60 V nm^{-1} (4). Helium (He) gas, neon (Ne) gas, or a mixture of He and Ne gases are used to image individual atoms, utilizing the phenomenon of field ionization (5–10). In these high **E**-fields, He or Ne atoms are field ionized, 45 Vdc nm^{-1} for He and 35 Vdc nm^{-1} for Ne, above individual surface atoms. This is because the outermost electron of the imaging gas atoms

quantum-mechanically tunnels into a sharply pointed microtip at the site of an atom. This creates a small diameter cone of He^+ or Ne^+ ions emanating from individual surface atoms; the total current from a tip with an area of $\sim 10^{-14}$ m^2 is $\sim 10^{-9}$–10^{-8} A, and hence the current from a single atom is $\approx 10^{-14}$–10^{-13} A, respectively (11). The field-ionized He^+ or Ne^+ ions are then accelerated along **E**-field lines that are orthogonal to the equipotentials associated with a tip, and they terminate on a detector, which is at Earth potential. The energetic ions are ultimately converted into visible light, employing a microchannel plate (MCP), which is the solid-state analog of an array of photomultiplier tubes, with a gain of 10^6 to 10^7 for a single ion. The detection efficiency of an MCP is equal to its open area, ~50–60%, which is a weak link in the detection system and needs to be improved in the future. In the FIM mode of operation, approximately 10^4 to 10^5 surface atoms are imaged, and the FIM images often exhibit the symmetry of the crystal lattice of the specimen. Thus, the physical basis of "seeing" atoms in direct space involves the quantum-mechanical process of field ionization of imaging gas atoms, which Oppenheimer (5) in 1928 first analyzed for a hydrogen atom in free space in a potential gradient of 10^2 Vdc m^{-1}. He calculated the time to ionize an atom at this value of **E** to be 10^{100} s, which is a googol (12), whereas in an FIM the time for field ionization is $<10^{-10}$ s. The **E**-field-ionized He^+ or Ne^+ gas ions are the messengers that allow us to observe individual atoms on the surface of a sharply pointed specimen in direct space with excellent atomic resolution (13). This is a singular intellectual and scientific achievement with tremendous ramifications for solving important scientific and technological problems in materials research.

Field evaporation: the sublimation of an atom from the surface of an APT tip caused by a high electric field

Subsequently, in 1956 Müller discovered the important physical phenomenon of field evaporation (or field desorption), which is the sublimation of atoms as ions from a microtip (radius <40 nm) specimen employing a high **E**-field that may be greater or less than the **E**-field necessary to ionize a He or Ne atom at a given cryogenic temperature. Müller observed this phenomenon by increasing the dc voltage on a W specimen and concomitantly increasing the value of **E**. Müller noticed that the atoms at the surface of a microtip are continuously evaporating (subliming) as ions, thereby exposing the interior of a specimen; hence this phenomenon was termed field desorption or field evaporation (14–17). Field evaporation is sublimation with the aid of an **E**-field and is a material-dependent property; for example, for W, the evaporation field ($\mathbf{E_e}$) is 57 V nm^{-1}, whereas for Ag, $\mathbf{E_e}$ is 25 V nm^{-1} at 0 K (18). Field evaporation is controlled by superimposing high-voltage pulses (V_{pulse}) on top of V_{ex}, where the pulse fraction (V_{pulse}/V_{ex}) is typically between 0.1 to 0.2; the optimum value is found empirically. In this manner the internal atomic structure of a specimen is routinely observed directly and reconstructed in 3-D to reveal imperfections, that is, atomic-scale defects such as vacancies (19, 20), self-interstitial atoms (21–23), chemical impurity atoms, dislocations (24, 25), stacking faults (26, 27), subboundaries, grain boundaries, clusters of atoms, and precipitates.

An historic and seminal short course and workshop on FIM were held at the University of Florida in Gainsville on March 14–22, 1966. There, review and original articles were presented on both the theory and application of FIM to problems in materials science requiring atomic-scale resolution. The results appearing in these proceedings demonstrated unequivocally the tremendous power of FIM for

obtaining quantitative information on an atomic scale (28). FIM has played an important role in many areas of materials research. For example, in radiation damage in metals FIM can be used (*a*) to study in situ point defects, point-defect clusters, and displacement cascades; (*b*) at temperatures as low as 12 K; (*c*) in quantitative detail; and (*d*) to obtain physically important information that is unattainable by any other experimental technique (29–33). FIM experiments have also provided detailed and quantitative atomic-scale information about the mechanisms of adatom surface diffusion, which are truly unique (34–38).

Displacement cascade: is produced by an energetic implanted particle and is the spatial array of vacancies and self-interstitial atoms

APFIM: atom-probe field-ion microscope

TOF: time of flight

Atom-Probe Field-Ion Microscopy

The next major advance in instrumentation occurred in 1968, when Müller, Panitz & McLane invented the atom-probe field-ion microscope (APFIM) (39), which consists of an FIM plus a special time of flight (TOF) mass spectrometer with the ability to detect single pulsed field-evaporated ions. An APFIM utilizes controlled pulsed field evaporation to determine the TOFs of individual ions, thereby determining their mass-to-charge state (m/n) ratios and hence their chemical identities, which is the ultimate in chemical analysis. A simple calibration procedure allows one to determine accurate quantitative values of m/n for all elements and their isotopes in the periodic table (40). Originally the TOFs were measured using two oscilloscopes, one for low Z-number elements and a second one for high Z-number elements, and Polaroid film was used to record each TOF event. This procedure was extremely tedious to record and analyze a statistically significant number of TOF events. This situation changed radically and permanently in 1975 with the interfacing of an APFIM at Cornell University to a Data General Nova computer with 8 K of discrete memory (41–43). The APFIM is a revolutionary instrument because it combines atomic-resolution FIM images with TOF mass spectrometry. It has been applied to a wide range of problems in materials science and engineering that cannot be studied by any other technique (44–49).

Atom-Probe Tomography

In 1973, Panitz invented the progenitor of all APTs, which is now called an imaging atom probe (50–52). It is my opinion that Panitz should receive more recognition for this major contribution than he has in the past. The next important form of an APT was the development of the position-sensitive atom probe (PoSAP) in 1988, which Cerezo et al. (53) invented as a serial instrument; its serial detection character was its major limitation as a practical research instrument. Kindbrisk later commercialized a parallel version of this APT, incorporating a reflectron lens; subsequently, Kindbrisk was purchased by the Polaron Group and renamed Oxford Nanosciences. Blavette et al. (54) designed and fabricated the first parallel APT in 1993 at Université de Rouen. This instrument is currently marketed by Cameca of Gennevilliers, France (**http://www.cameca.fr/html/product_atom_probe.html**) and in its present incarnation is called a laser-assisted wide-angle tomographic atom probe (LA-WATAP). The optical position-sensitive atom probe (55) is a parallel instrument that

utilizes optical detection as opposed to charge detection; the optical detection mode is no longer widely employed. In 2006, Oxford Nanosciences was acquired by Imago (**http://www.imago.com/imago/**), and hence there are now only two manufacturers of APTs, Imago Scientific Instruments (Madison, Wisconsin) and Cameca. The commercial APTs can readily reconstruct a lattice of atoms in 3-D with their chemical identities (m/n values) (56) and analyze the 3-D reconstructed structure with sophisticated software programs. The detailed technical specifications of the two APTs as well as the capabilities of their data analysis programs differ.

LEAP^{TM}: local-electrode atom probe

LE: local electrode

The spatial depth resolution for chemical analysis is the {hkl} interplanar spacing (<0.1 nm), along the [hkl] direction being analyzed, and the lateral resolution is 0.3 nm to 0.5 nm within an {hkl} atomic plane. Additionally, TOF mass spectrometry employing an MCP as the primary detector has the distinct advantage that the detection sensitivity is identical for all elements and their isotopes in the periodic table once the energy of an ion is greater than 3 kV. Moreover, the mass resolution ($m/\Delta m$) is excellent for light elements of the periodic table, implying that it is easy to distinguish, for example, $^{1}H^{+}$ from the $^{3}He^{+}$ and ^{4}He isotopes in mass spectra (57–60). Furthermore, APT can perform quantitative chemical analyses without standards because Nature kindly provides us with internal standards in the form of handbook values of the isotopic abundances.

Recently, a so-called local-electrode atom-probe (LEAP^{TM}) tomograph was developed and commercialized by Imago Scientific Instruments (61). The original idea for employing a local electrode (LE) came from Nishikawa & Kimoto (62), who employed an LE in a scanning atom probe (SAP). In an SAP, the LE is scanned from microtip to microtip to maximize the amount of data that can be obtained in a given period of time and to determine chemistry on the atomic scale over a several-millimeter length scale. Imago Scientific Instrument's revolutionary LEAP 3000X Si X^{TM} metrology system employs an LE with a 30-μm-diameter orifice. The LE is typically placed within ~30 μm of a sharply pointed microtip (local radius of <20 nm) specimen; the close proximity of the microtip to the LE's orifice decreases the value of V_{ex} needed to achieve a given value of **E**. **Figure 1** exhibits a schematic diagram of a 3-D LEAP^{TM} tomograph operating in the scanning mode. An array of microtip specimens sits on a conducting substrate, which is maintained at a positive potential, V_{ex}. To field evaporate atoms as ions, the LE is pulsed with a negative potential, V_{pulse}, which increases the value of the local **E**-field at the microtip specimen to the requisite value for field evaporation of ions. The complete position-sensitive detector consists of a primary detector in the form of an MCP, behind which is a delay-line detector. The MCP measures the TOF of an ion, and the delay-line detector measures its x- and y-coordinates. The TOFs and x- and y-coordinates of individual atoms in a crystallographic {hkl} plane in a specimen are hence determined on an atom-by-atom basis, using this composite detector. The physical phenomenon of field evaporation allows one to access the interior of a microtip specimen, and in this manner sophisticated software programs can determine and reconstruct in 3-D the positions of all atoms and their m/n values for a given volume of material. For example, a data set of 480×10^{6} atoms corresponds to a volume of $\sim 8 \times 10^{-21}$ m^{3} (8×10^{6} nm^{3}). Data sets from different specimens can, of course, be combined to examine larger volumes of

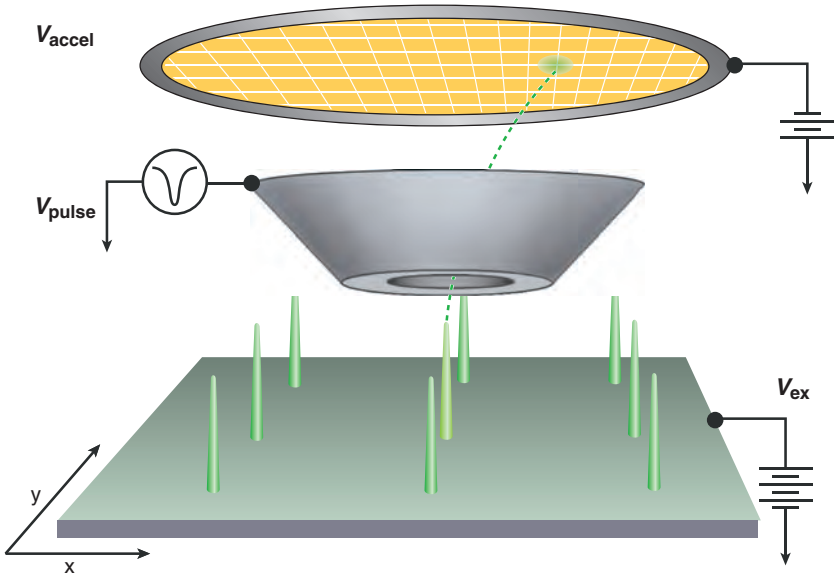

Figure 1

Schematic drawing of a 3-D local-electrode atom-probe (LEAP^{TM}) tomograph. The substrate is maintained at a positive potential, V_{ex}, which supports the microtip specimens; the substrate can be translated in the x-y plane to scan from specimen to specimen. The local electrode is pulsed with a negative voltage, V_{pulse}, to increase the electric field (**E**) at a microtip specimen to the requisite value to field evaporate atoms as ions. Figure courtesy of Prof. Lincoln Lauhon, Northwestern University.

material and to improve the counting statistics. The LEAP 3000X Si X^{TM} includes electrical pulsing; the pulse repetition rate is variable in discrete steps from 1 kHz to 250 kHz, and a detection rate of up to 2×10^6 ion min^{-1} (120×10^6 ion h^{-1}) can be achieved. This implies that a data set containing 10^9 atoms can be obtained in $8^1/_3$ h from a single cooperative specimen. For electrical pulsing, the full-width half-maximum (FWHM) value of m/Δm is 500 and the full-width tenth-maximum (FWTM) value of m/Δm is 180 for $^{27}Al^+$, with the tip at its maximum distance from the detector.

Alternatively, the LEAP 3000X Si X^{TM} operates using a pulsed picosecond laser (green light) to field evaporate ions. The exact mechanism by which laser-induced evaporation of atoms occurs is currently a subject of a scientific debate (63, 64). The two suggested physical mechanisms are (*a*) evaporation (sublimation) over a Schottky hump assisted by the **E**-field component of the laser beam and (*b*) heating of a microtip specimen by the laser beam with an energy per pulse that is typically less than 5 nJ. The heating mechanism implies that an atom is thermally excited over the Schottky hump produced by the applied V_{ex}; the evidence for this mechanism is strong (J. Bunton, Imago Scientific Instruments, unpublished observations). **Figure 2** illustrates how the LEAP^{TM} tomograph functions when green laser light is used to evaporate (sublime) atoms as ions.

To a first order, the interpretation of mass spectra is independent of the physical mechanism of laser-induced evaporation. For the LEAP 3000X Si X^{TM}, the laser pulse repetition rate is variable in steps from 1 kHz to 500 kHz, and a detection rate of up to 5×10^6 ion min^{-1} (300×10^6 ion h^{-1}) can be obtained. Therefore, a data set containing 10^9 atoms is attainable from a single very cooperative specimen in $3^1/_3$ h, which is a factor of 2.5 faster than with electrical pulsing. For laser pulsing, the

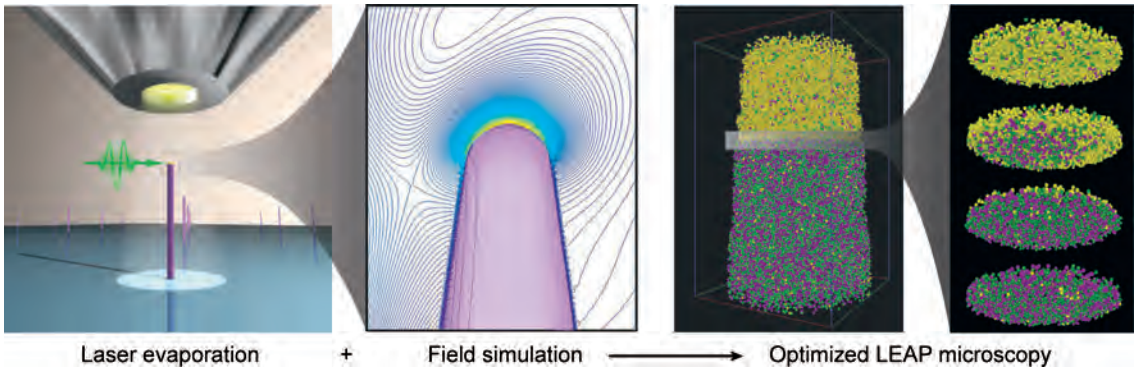

Figure 2

(Left) An array of microtips sitting on a conducting substrate with green laser light impinging on a single microtip. (Middle) The calculated electric field at a microtip that results from the **E**-component of the laser beam. Courtesy of Prof. Tamar Seideman (Chemistry Department, Northwestern University). (Right) The results of an analysis of an InAs nanowire grown by the vapor-liquid-solid (VLS) technique.

FWHM value of m/Δm is 1200, and the FWTM value of m/Δm is 300 for $^{27}Al^{+}$, with the microtip specimen at its maximum distance from the detector. The dispersion of the ions' momenta is smaller for laser pulsing because when the ions surmount the Schottky hump they have a thermal energy k_BT, where k_B is Boltzmann's constant and T is the absolute temperature in degrees Kelvin. Therefore, the spread in the momenta (TOFs) is smaller than for electrical pulsing, resulting in larger values of m/Δm. The LEAP 3000X Si X^{TM} is a straight TOF instrument. Hence, the value of m/Δm is ultimately limited by the spread in momenta of the field-evaporated ions for either electrical or laser pulses. For both electrical and laser pulsing the maximum cross-sectional area of a microtip specimen analyzed is 200 nm × 200 nm, at the minimum distance from the MCP detector, 90 mm.

A commonly used solution to improve m/Δm is a single-stage reflectron lens, which is isochronous and can yield m/Δm values of >1500 for either electrical or laser pulsing if the so-called energy deficits are small (65, 66). The primary limitation of using a reflectron lens is its small field of view (FOV) (approximately 20 nm × 20 nm), for example, in the PoSAP. Recently, however, a wide acceptance-angle reflectron lens has been designed and commercialized; this lens has an FOV of 100 nm × 100 nm, an FWHM m/Δm value of 600, and an FWTM m/Δm value of 300 for $^{27}Al^{+}$, using voltage pulses; with laser pulsing, the FWHM m/Δm value is 2500 and the FWTM m/Δm value is 1000 for $^{27}Al^{+}$. An APT with a wide acceptance-angle FOV reflectron lens is commercially available from Imago Scientific Instruments and is denoted as a 3DAP-X. This instrument is capable of electrically pulsing specimens at 0.4 kHz to 20 kHz and laser pulsing them at 1 kHz to 200 kHz, with a maximum data collection rate of 1.8×10^5 ion min^{-1} (10.8×10^6 ion h^{-1}) for either electrical or laser pulsing. Thus, there is now a choice of commercial APTs available with different technical specifications and, of course, different prices.

FOV: field of view

A Comparative Example of the Capabilities of a Conventional Atom-Probe Tomograph and a 3-D LEAP™ Tomograph

To illustrate the differences between a conventional APT and an earlier version (November 2002) of a 3-D LEAP™ tomograph, we present results for a Ni–5.2 at.% Al–14.2 at.% Cr at.% alloy, which was aged for 256 h at 873 K to produce $\gamma'(L1_2$ structure)-precipitates in a γ(f.c.c.) matrix (see below for additional results on this alloy). At 256 h, the γ'-precipitates were analyzed with conventional APT and LEAP™ tomography, which both employ electrical pulsing (**Figure 3**). The conventional APT analysis ($16 \times 16 \times 195$ nm^3 or 4.99×10^4 nm^3) partially intersects 23 γ'-precipitates in a 36-h analysis and contains 1.8×10^6 atoms; the pulse repetition rate was 1.5 kHz. The LEAP™ tomographic analysis ($86 \times 86 \times 63$ nm^3 or 4.66×10^5 nm^3) fully intersects 50 γ'-precipitates and partially intersects 20 γ'-precipitates, detecting 9.8×10^6 atoms after a collection period of 0.8 h. This did not

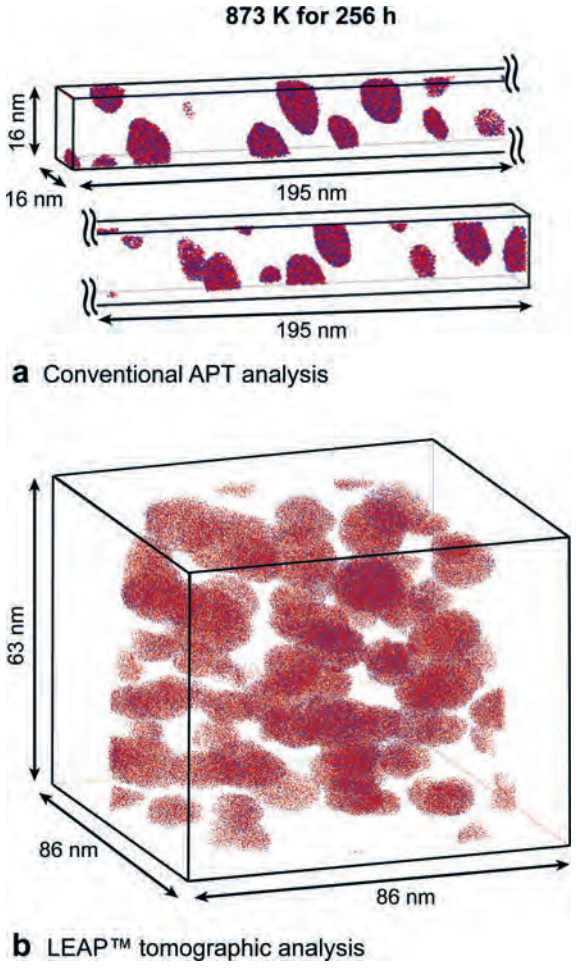

Figure 3

Specimens of Ni–5.2 Al at.%–14.2 Cr at.% aged at 873 K for 256 h were analyzed with (*a*) conventional APT and (*b*) LEAP™ tomography. The $16 \times 16 \times 195$ nm^3 (4.99×10^4 nm^3) and $86 \times 86 \times 63$ nm^3 (4.66×10^5 nm^3) volumes contain approximately 1.8×10^6 and 9.8×10^6 atoms, respectively. Only Al (red) and Cr (blue) atoms within γ'-precipitates are displayed for the sake of clarity. Each dot represents a single atom. From Reference 91.

push this instrument's limits: The pulse repetition rate was 200 kHz. 3-D imaging by LEAP^{TM} tomography does not suffer from the same projection effects associated with transmission electron microscope (TEM) imaging, which is a 2-D projection of a 3-D object. As **Figure 3** shows, classical APT is limited to smaller analyzed volumes, typically $15 \times 15 \times 100$ nm^3 or 22,500 nm^3. In contrast, LEAP^{TM} tomographic analyses are presently capable of analyzing volumes greater than $200 \times 200 \times 200$ nm^3 or 2×10^6 nm^3 in a significantly shorter time.

TEM: transmission electron microscope

Thus, we are currently in a new era in atom-probe tomographic instrumentation, in which the detection sensitivity of an element is one atomic part per million for a data set of 100×10^6 atoms, with a small experimental uncertainty, for both electrical and laser pulsing because significantly larger volumes of material can be analyzed in radically short time periods. The results obtained to date using LEAP^{TM} tomography represent a dramatic improvement over the earlier APTs. Thus, LEAP^{TM} tomography is a revolutionary technological achievement with significant ramifications for future materials science and engineering research.

APPLICATIONS

Heterophase Interfacial Segregation on an Atomic Scale

Structural alloys typically contain multiple alloying elements whose interactions govern the formation of strengthening phases, partitioning behavior between the phases, and segregation at internal heterophase interfaces. The combination of HREM and APT has recently made it possible to measure the compositional variations with near-atomic-scale resolution. The combined application of such characterization techniques with first-principles computational methods provides the basis for greatly expanded insight into the microscopic factors governing compositional variations in multicomponent alloys. The research reviewed herein employs this combined approach in a study of Mg in two-phase Al-Sc-Mg alloys. We present measurements of Mg composition profiles at the subnanoscale level, which are compared with the predictions of first-principles calculations. These calculations establish a pronounced electronic driving force for the segregation of Mg to coherent α-Al (f.c.c.)/Al_3Sc ($L1_2$) interfaces in this model two-phase ternary alloy system.

We focus on an Al–2.2 at.% Mg–0.12 at.% Sc alloy, which is relevant for aerospace and marine applications (67) and as a model system for its microstructural applications. The alloy was prepared employing solidification and homogenization procedures described elsewhere (68, 69). During aging at 300°C, the supersaturated solid solution decomposes into an α-Al (f.c.c.) matrix and a high number density ($4 \pm 2 \times 10^{22}$ precipitate m^{-3}) of nanoscale Al_3Sc precipitates with radii of less than 4.5 nm. HREM observations demonstrate that the α-Al (f.c.c.)/Al_3Sc ($L1_2$) interface remains coherent, that is, there are no interfacial misfit dislocations, for both the binary Al–0.18 at.% Sc and ternary Al-Sc-Mg alloys, even for the largest precipitates. Without Mg, the precipitate exhibits pronounced facets on the {100}, {110}, and {111} planes (**Figure 4*a***), which tend to shrink (**Figure 4*b***) with the addition of Mg, and the precipitate has a tendency to become spheroidal. The reduction of {100} facet lengths

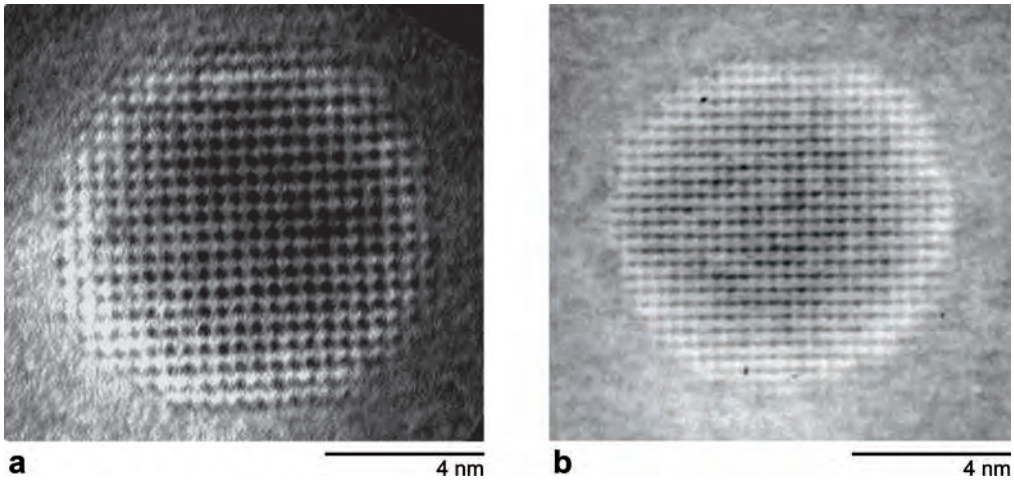

Figure 4

HREM images ([100] zone axis) of Al_3Sc precipitates in (*a*) Al–0.18 at.% Sc alloy after aging at 300°C for 350 h and (*b*) Al–2.2 at.% Mg–0.12 at.% Sc after aging at 300°C for 1040 h. From Reference 86.

with the addition of Mg suggests a decrease in the crystallographic anisotropy of the interfacial free energy and the possibility of appreciable interfacial segregation.

We investigated this behavior further, employing detailed APT measurements of solute composition profiles. The spatial resolution of the APT is illustrated in **Figure 5*a***, where an analysis performed near the 110 crystallographic pole reveals the {220} atomic planes perpendicular to the analysis direction. The curvature of the reconstructed planes comes from the projection of the hemispherical tip onto a planar detector. In the Al_3Sc precipitate, alternating planes containing 100% Al and 50% Al are visible, consistent with the $L1_2$ structure of the Al_3Sc phase. A proximity histogram calculates the average composition in shells of 0.4-nm thickness at different distances from the α-Al (f.c.c.)/Al_3Sc ($L1_2$) interface: The interface is defined by an isoconcentration surface corresponding to 18 at.% Sc (**Figure 5*b***) (70). Interfacial Mg segregation was observed for all analyzed aging times, and the particular example of **Figure 5*c*** exhibits a Mg concentration enhancement of 180% at the heterophase interface. The maximum interface Mg concentration decreases slightly during the early aging times and then remains constant within experimental error, which indicates that a stationary state has been achieved at least locally.

To investigate the microscopic factors governing the pronounced interfacial enhancement of Mg, we employed the theoretical framework provided by a model of diffusion-limited precipitate growth kinetics. The validity of such a model is supported by studies of coarsening kinetics in both binary Al-Sc (68, 69, 71, 72) and ternary Al-Sc-Mg alloys. We interpret the concentration profiles measured by APT as representing stationary-state solutions to the diffusion equation, subject to the boundary conditions imposed by local thermodynamic equilibrium and flux balance (e.g., Reference 73). For spherical precipitate geometries, employing a mean-field,

Stationary state: implies that the concentrations (c_i) of the different components (i) in a system do not change with time, $(\frac{\partial c_i}{\partial t}) = 0$

Coarsening: occurs when a two-phase system is in a stationary state and the number density of precipitates decreases with increasing aging time at a constant volume fraction of precipitates

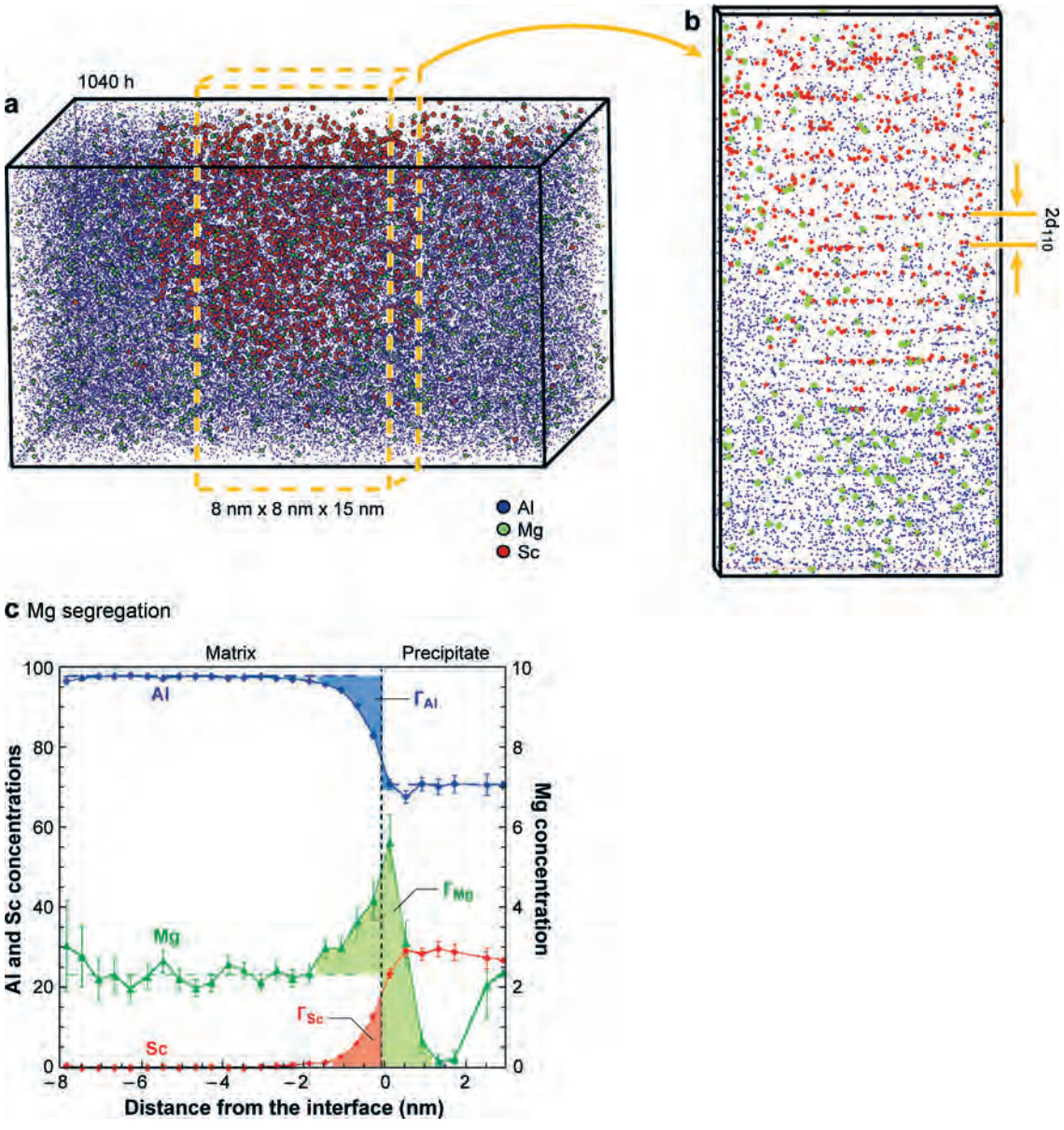

Figure 5

(*a*) 3-D reconstruction of an analyzed volume from a specimen aged at 300°C for 1040 h showing the isoconcentration surface used to define the α-Al/Al_3Sc heterophase interface. (*b*) 3-D reconstruction of an Al_3Sc precipitate with a slice taken through the precipitate displaying the {110} planes. (*c*) Proximity histogram showing Al, Mg, and Sc concentrations from the α-Al/Al_3Sc interface. Data visualization performed using Northwestern University's ADAM 1.5 software package (70). From Reference 86.

stationary-state solution to the diffusion equation (neglecting off-diagonal terms in the diffusion matrix), one can derive interface compositions from the following equations (i = Al, Sc, Mg):

$$\mu_i^{\alpha}\left(\hat{x}_{\mathrm{Mg}}^{\alpha},\ \hat{x}_{\mathrm{Sc}}^{\alpha}\right) - \mu_i^{\alpha'}\left(\hat{x}_{\mathrm{Mg}}^{\alpha'},\ \hat{x}_{\mathrm{Sc}}^{\alpha'}\right) = \frac{2\sigma}{R}\bar{V}_i, \qquad 1.$$

$$\frac{\hat{x}_{\mathrm{Sc}}^{\alpha'} - \hat{x}_{\mathrm{Sc}}^{\alpha}}{\hat{x}_{\mathrm{Mg}}^{\alpha'} - \hat{x}_{\mathrm{Mg}}^{\alpha}} = \frac{D_{\mathrm{Sc}}}{D_{\mathrm{Mg}}}\frac{\hat{x}_{\mathrm{Sc}}^{\alpha} - \hat{x}_{\mathrm{Sc}}^{\infty}}{\hat{x}_{\mathrm{Mg}}^{\alpha} - \hat{x}_{\mathrm{Mg}}^{\infty}}, \qquad 2.$$

where $\hat{x}_{\mathrm{Sc}}^{\alpha}$, $\hat{x}_{\mathrm{Mg}}^{\alpha}$, $\hat{x}_{\mathrm{Sc}}^{\alpha'}$, and $\hat{x}_{\mathrm{Mg}}^{\alpha'}$ denote mole fractions of Sc and Mg on the Al(α) and Al_3Sc(α') sides of the interface for a precipitate of radius R, σ is the heterophase interfacial free energy, the variables μ_i^{α} and $\mu_i^{\alpha'}$ represent bulk chemical potentials, and $\bar{V}_i$ is the partial molar volume for species i in the precipitate phase. The variables $\hat{x}_{\mathrm{Sc}}^{\infty}$ and $\hat{x}_{\mathrm{Mg}}^{\infty}$ denote far-field solute concentrations. The first three equations (Equation 1) correspond to the Gibbs-Thomson conditions incorporating the effect of capillarity in the formulation of the conditions for local thermodynamic equilibrium, whereas Equation 2 reflects the constraint imposed by solute-flux balance at the precipitate/matrix interface.

Table 1 lists values of the interface concentrations calculated from Equations 1 and 2 for precipitates of radii 2 nm and 4 nm at an aging temperature of 300°C. For comparison, we list compositions corresponding to two-phase equilibrium between bulk ($R \rightarrow \infty$) α- and α'-phases in the ternary alloy Al–2.2 at.% Mg–0.12 at.% Sc considered experimentally. Because experimental values for the chemical potentials in the ternary Al_3Sc intermetallic phase are unavailable, we employed first-principles bulk free-energy models in the calculations of equilibrium phase compositions. The bulk free energies were derived within a model of noninteracting substitutional defects, following the approach outlined in References 74–76. In the evaluation of Equation 2, we employ APT-measured values of $\hat{x}_{\mathrm{Sc}}^{\infty} = 0.025 \pm 0.007$ at.% and $\hat{x}_{\mathrm{Mg}}^{\infty} = 2.3 \pm 0.007$ at.%. The solute diffusivities in Al are $D_{\mathrm{Sc}} = 8.84 \times 10^{-20}$ m^2 s^{-1} (77) and $D_{\mathrm{Mg}} = 1.62 \times 10^{-16}$ m^2 s^{-1} (78) at the aging temperature. Additionally, the value $\sigma = 0.175$ J m^{-2} was derived from first-principles calculations (79). Values of the interface compositions for precipitates with finite radii were derived by linearizing the concentration dependencies of Equations 1 and 2 about the bulk compositions. By comparing the results in the first two rows of **Table 1** with those corresponding to bulk phases (final row), we see that the effects of capillarity and solute-flux balance are estimated to give rise to relatively small (≈10%) changes in the matrix

Table 1 Interface solute concentrations (at.%) calculated from Equations 1 and 2 for spherical (α') Al_3Sc precipitates of radius R in a supersaturated (α) matrix in Al-Sc-Mg

R (nm)	$\hat{x}_{\mathrm{Sc}}^{\alpha}$	$\hat{x}_{\mathrm{Mg}}^{\alpha}$	$\hat{x}_{\mathrm{Sc}}^{\alpha'}$	$\hat{x}_{\mathrm{Mg}}^{\alpha'}$
2	2.5×10^{-4}	2.2	25	3.4×10^{-7}
4	1.8×10^{-4}	2.2	25	4.0×10^{-7}
∞	9.0×10^{-5}	2.4	25	4.8×10^{-7}

Mg concentration at the growing precipitate/matrix heterophase interface. Thus, the pronounced interfacial enhancement of Mg measured by APT cannot be interpreted simply as reflecting the effects of capillarity and solute flux balance in a model of diffusion-limited precipitate growth. Additional first-principles calculations suggest instead that the segregation of Mg observed by APT reflects equilibrium adsorption.

A reliable comparison between experiment and theory can be made in terms of the integrated area under the Mg concentration profiles. Specifically, the relative Gibbsian interfacial excess of Mg (Γ^{rel}_{Mg}) can be employed to derive a quantitative measure of the degree of equilibrium segregation in this ternary alloy. The quantity Γ^{rel}_{Mg} can be calculated from Γ_{Mg}, Γ_{Sc}, and Γ_{Al}, as described in References 80 and 85. We estimate these excess values for Al (negative value) and Mg and Sc (positive values) as the areas under the curves in **Figure 5*c*** (81–83). This analysis yields $\Gamma^{rel}_{Mg} = 1.9 \pm 0.5$ atom nm^{-2}. By comparison, Γ^{rel}_{Mg} derived from the calculated composition profiles is 1.2 atom nm^{-2}. The close agreement between experiment and theory strongly supports the conclusion that the measured interfacial enhancement of Mg reflects pronounced equilibrium segregation of this species at coherent α-Al/Al_3Sc heterophase interfaces. From the Gibbs adsorption isotherm theorem, we estimate that Mg segregation leads to a 0.01 J m^{-2} reduction in σ. Equilibrium interfacial segregation of Mg thus should reduce slightly (by approximately 5%) the rates of precipitate coarsening in Al-Sc-Mg relative to binary Al-Sc (84, 85). First principles also showed that the driving force for segregation is primarily electronic (chemical) and not elastic (86). Reference 87 provides further details concerning Mg segregation at coherent α-Al/Al_3Sc heterophase interfaces. The research described above demonstrates the power of combined APT and HREM experiments, first-principles calculations, and theory in obtaining deep physical insights into a complex problem at the same length scales for a similar number of atoms.

Gibbsian interfacial excess of solute: a basic thermodynamic quantity that quantifies the excess concentration of solute at an interface

Coherent heterophase interface: a 2-D interface between two phases that does not contain misfit dislocations

Ni_3Al ($L1_2$): has Ni atoms at the centers of the six faces of a cube and eight Al atoms at its corners

Kinetic Pathways of Decomposing Ni-Al-Cr Alloys

Ni-based superalloys are used to fabricate single-crystal two-phase [$\gamma'(L1_2)$ and γ(f.c.c.)] turbine blades for aeronautical jet engines, both commercial and military, and commercial land-based gas-turbine engines for generating electrical power; a single unit can generate as much as 500 MW. The single-crystal two-phase turbine blades are directionally solidified from different commercial or proprietary Ni-based superalloys and contain 10 or more alloying elements. There is a continuing effort to increase the operating temperature of these turbine blades to increase the thermodynamic efficiency of the engines, thereby reducing fuel consumption, which implies, among other things, improving the high-temperature creep and oxidation resistance of these Ni-based superalloys. One route to improving the creep resistance is to decrease the coarsening rate (Ostwald ripening) of the coherent $\gamma'(L1_2)$-precipitates, which can constitute more than 60% by volume of the turbine blades. Both the creep resistance and maximum operating temperature are improved by alloying with high-melting-point refractory elements, such as tungsten, molybdenum, rhenium, and ruthenium.

These refractory elements have small values of their diffusivities, which retards the rate of coarsening, $d\langle R\rangle/dt$, of the $\gamma'(L1_2)$-precipitates; $\langle R\rangle$ is the average precipitate

Decomposition of an alloy: a first-order phase transformation that involves the nucleation, growth, and coarsening of a second phase from a solid solution

radius. To understand the roles played by these refractory elements in quantitative detail, we are studying model Ni-based superalloys based on ternary Ni-Al-Cr alloys with different concentrations of Al and Cr, to which we add, one element at a time, refractory elements (Re, W, Ta, Nb, or Ru) to produce quaternary, quinary, or sexinary alloys. In this manner, we are able to unravel the role played by each refractory element on the kinetic pathways leading to the final nanostructure.

We studied in detail the kinetic pathways of the different stages of precipitation of ordered γ'-precipitates ($L1_2$) in Ni–5.2 at.% Al–14.2 Cr at.% at 873 K (88–93). Precipitates with radii as small as 0.45 nm are fully characterized by APT. Contrary to what is often assumed in modeling coarsening (Ostwald ripening), the average composition of γ'-precipitates evolves temporally. Power-law time dependencies of the number density, N_v, $\langle R \rangle$, and the absolute values of the supersaturations, $|\Delta c_i|$, of Al and Cr are determined and compared with coarsening models. The formation of γ'-precipitates from a supersaturated γ-matrix in a temperature range for which nucleation and growth are observable has been studied in binary Ni-Al alloys by direct (94–96) and indirect (97) imaging techniques. We employ APT to characterize a specific ternary alloy fully (98, 99). The experimental procedures are described elsewhere (100, 101).

After homogenization, Ni–5.2 at.% Al–14.2 Cr at.% decomposes at 873 K into a high N_v of nanometer-sized, spheroidal γ'-precipitates via a first-order phase transformation. Misfit between the γ- and γ'-phases is nearly zero, and therefore the γ'-precipitates are coherent and spheroidal to 1024 h, the maximum time we employed (91). The γ'-precipitates are first observed after 0.17 h of aging [prior to this time we observed short-range order but no detectable γ'-precipitates (92)], and the $\langle R \rangle$ and volume fraction, V_f^{γ}, values of the γ'-precipitates are determined to be 0.74 nm and 0.11% (**Figure 6**). A sharp rise in N_v at a constant $\langle R \rangle$ value is observed between aging times of 0.17 h and 0.25 h, indicating that nucleation is occurring. APT-detected γ'-precipitates are as small as $R = 0.45$ nm (20 detected atoms). After 0.25 h and until 256 h, precipitate coagulation and coalescence are observed, as seen at 4 h in **Figure 7**. Given the small $\langle R \rangle$ and small lattice parameter misfit values, this is not the result of elastically driven particle migration and marks the finest scale, as well as smallest V_f^{γ}, for which this phenomenon has been observed in the solid state. The peak value of N_v, $(3.2 \pm 0.6) \times 10^{24}$ m^{-3}, is achieved after 4 h of aging, after which the transformation enters a quasi-steady-stationary regime with a constant power-law dependence of $t^{-0.64 \pm 0.06}$. In this regime, $V_f^{\gamma'}$ asymptotically increases toward its equilibrium value (upper panel in **Figure 6**), indicating that this first-order phase transformation is not complete, yet $\langle R \rangle$ has a temporal dependence of 0.29 ± 0.05, which is approximately consistent with the $t^{1/3}$ prediction for Ostwald ripening in a ternary alloy (102, 103).

The average compositions of the γ-matrix (top half of **Figure 8**) and γ'-precipitates continually evolve. The γ-matrix becomes more enriched in Ni and Cr and depleted in Al with increasing time. Between 4 h and 16 h, the solute far-field concentrations change slowly ($dc/dt \rightarrow 0$), and the quasi-stationary-state approximation is applied after 16 h. Assuming this approximation, Marquis & Seidman (85) determined the solid solubilities, c_i^{eq}, in a ternary Al-Sc-Mg alloy, utilizing $c_i(t) = \kappa t^{-1/3} + c_i^{eq.}$ Employing this approach, c_i^{eq} are 16.7 ± 0.4 at.% Al and

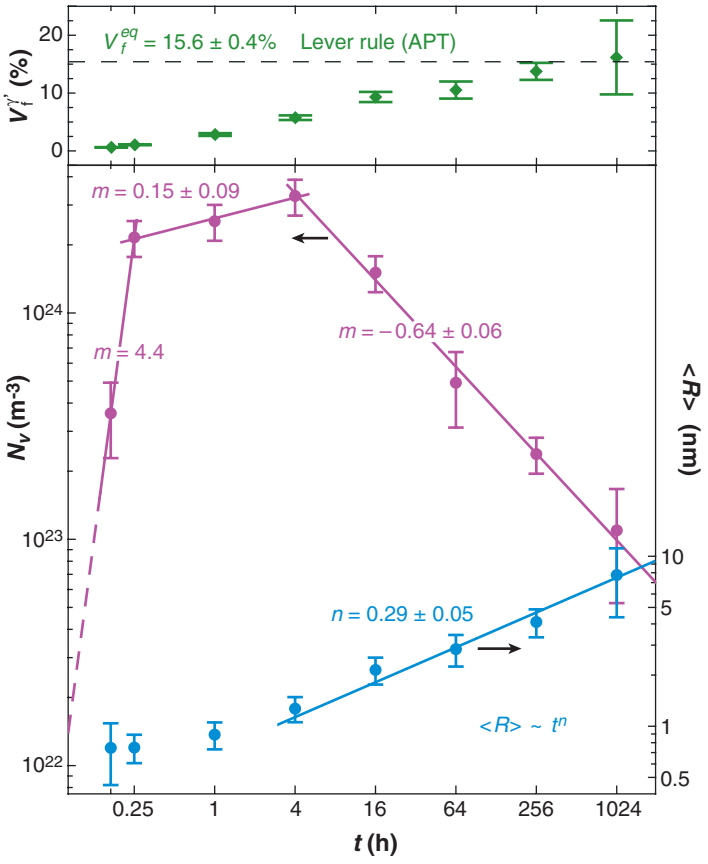

Figure 6

The temporal evolution of the γ′-precipitate volume fraction ($V_f^{\gamma'}$), number density (N_v), and average radius ($\langle R \rangle$) in Ni–5.2 at.% Al–14.2 Cr at.% aged at 873 K as determined by APT. Adapted from Reference 91.

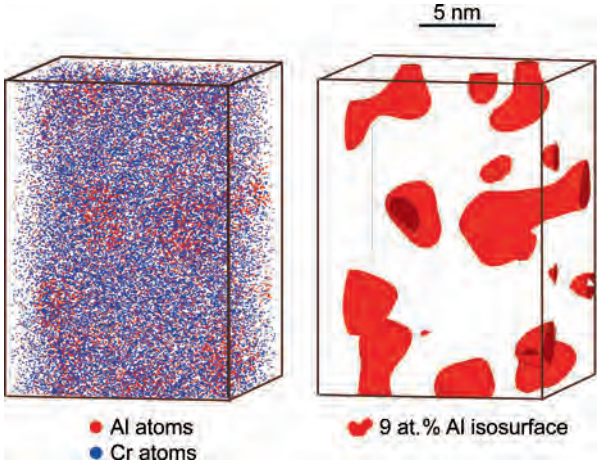

Figure 7

A subset (15 × 15 × 30 nm^3) of a conventional APT reconstructed volume of Ni–5.2 at.% Al–14.2 Cr at.% aged at 873 K for 4 h (Al and Cr atoms in the γ′-precipitates are displayed). A fraction, ~30%, of the γ′-precipitates, delineated by 9 at.% Al isoconcentration surfaces, is coalesced. Adapted from Reference 128.

Figure 8

The average far-field concentrations, c_i, and supersaturations, $|\Delta c_i|$, in the γ-matrix obtained by APT for Ni–5.2 at.% Al–14.2 Cr at.% aged at 873 K. Adapted from Reference 91.

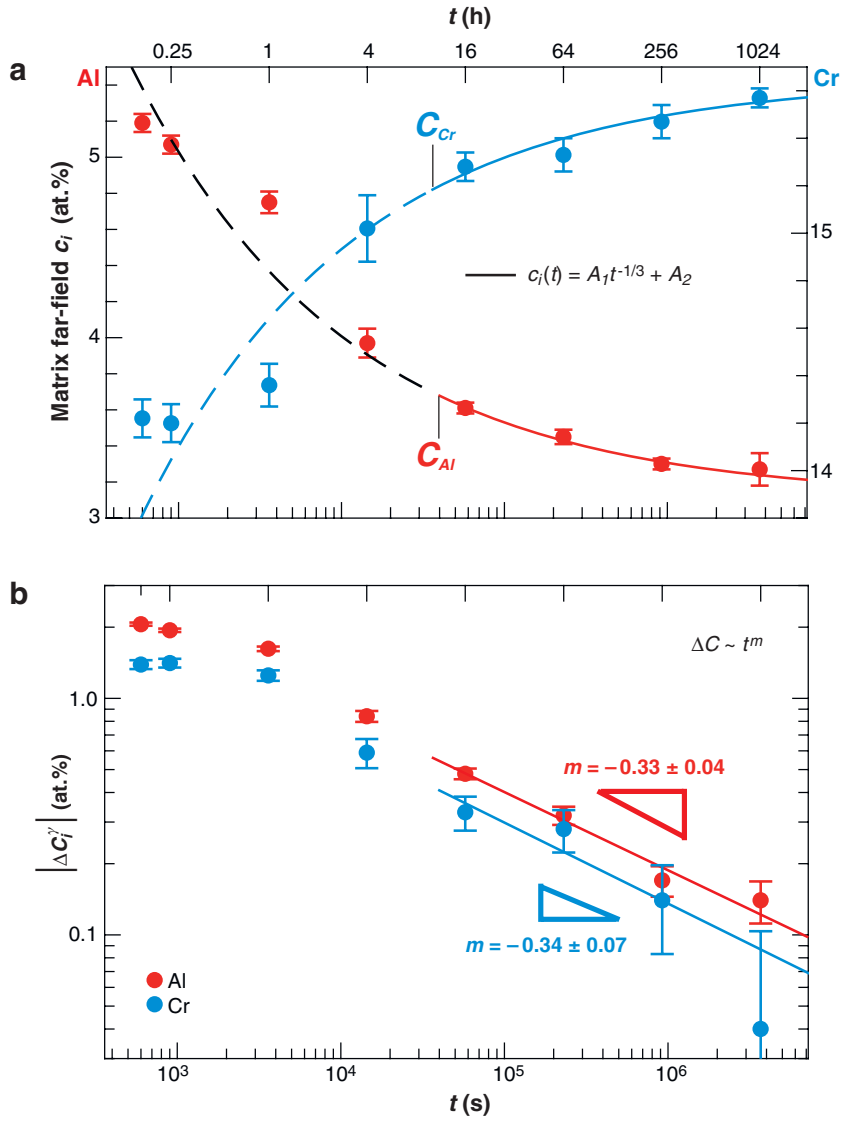

6.77 ± 0.30 at.% Cr for the Al-matrix within two standard deviations. Then the γ-matrix supersaturations, $\Delta c_i = c_i(t) - c_i^{eq}$, are determined (bottom half of **Figure 8**). Their temporal behavior is in approximate agreement with the prediction of $\Delta c \sim t^{-1/3}$ for Ostwald ripening. The classical theories of nucleation and growth assume that the composition of the γ'-precipitates is at their equilibrium value at a reaction's onset. Contrary to this assumption, the γ'-precipitates are supersaturated with Al (19.1 ± 2.8 at.%) and Cr (9.7 ± 2.1 at.%) at $t = 0.17$ h, which decrease continuously to 16.70 ± 0.29 at.% Al and 6.91 ± 0.20 at.% Cr at 1024 h. The equation for the evolving compositions, $c_i(t) = \kappa t^{-1/3} + c_i^{eq}$, fits the experimental data for the

γ'-precipitates. This fit yields equilibrium values of 3.13 $\pm$ 0.08 at.% for Al and 15.61 $\pm$ 0.18 at.% for Cr in the γ'-phase. Finally, via the lever rule, the equilibrium $V_f^{\gamma'}$ for the γ'-phase is 15.6 $\pm$ 0.4% (top panel in **Figure 6**).

Partitioning ratio: given by the ratio of element *i* in precipitating phase divided by the concentration of *i* in the matrix

To understand the role played by Re in model Ni-based superalloys, 2 at.% Re additions to a model Ni–10 at.% Al–8.5 at.% Cr alloy were studied with respect to its effects on the temporal evolution of the nanostructure and partitioning behavior of Ni, Al, Cr, and Re between the γ- and γ'-phases. Chemical evolution of this quaternary alloy aged at 1073 K from 0.25 h to 264 h was studied using APT (104, 105). The morphology of the γ'-precipitates remains spheroidal to 264 h. Our results demonstrate that Re significantly decelerates the coarsening of γ'-precipitates in comparison to a ternary Ni–10 at.% Al–8.5 at.% Cr alloy aged at 1073 K. Re may segregate to the γ/γ' interfaces and retard the coarsening of γ'-precipitates at elevated temperature, thereby increasing the creep resistance of Ni-based superalloys (106, 107). The results of this study are contrasted with results on Ni–10 at.% Al–8.5 at.% Cr and Ni–10 at.% Al–8.5 at.% Cr–2 at.% W alloys (108).

Spheroidal γ'-precipitates, $\langle R \rangle = 3.89$ nm, are observed in this as-quenched alloy owing to the high $|\Delta c_i|$ values of Cr and Al. The 3-D reconstruction of a volume of $16 \times 16 \times 130$ nm^3, containing $>1.5 \times 10^6$ atoms, confirms the presence of the γ'-precipitates in the as-quenched state, 0 h (**Figure 8**). In **Figure 9**, the partitioning behavior of all the elements is visualized through a 3-D reconstruction of the data. Al partitions, of course, to γ'-precipitates, whereas Ni, Cr, and Re prefer the γ-matrix. A fraction of the γ'-precipitates is interconnected by necks, which is indicative of a coagulation and coalescence coarsening mechanism.

Figure 10 displays 3-D reconstructions as a function of aging time, which clearly demonstrates the coarsening of the γ'-precipitates. Each reconstruction is a subset of results extracted from the entire volume to create a 10×10 nm^2 cross section for comparison as a function of aging time. **Figure 10** demonstrates qualitatively the increasing $\langle R \rangle$ values, and decreasing N_v values, of the γ'-precipitates with increasing aging time. Additionally, at the longest aging time of 264 h the morphology of the γ'-precipitates remains spheroidal and the $\langle R \rangle$ values are considerably smaller (31.5 nm) than those of the large cuboidal γ'-precipitates of ternary Ni–10 at.% Al–8.5 at.% Cr and quaternary Ni–10 at.% Al–8.5 at.% Cr–2 at.% W alloys (114 nm and 77 nm, respectively) (109). Therefore, the addition of Re stabilizes the precipitate morphology and significantly retards the coarsening kinetics of the γ'-precipitates in this Ni-Al-Cr-Re alloy.

An APT reconstruction of this Ni-Al-Cr-Re alloy (**Figure 9**) exhibits clearly the alternating Al-rich planes along the [100] analysis direction inside the γ'-precipitates, even in the as-quenched state. This is direct evidence that the γ'-precipitates have the ordered $L1_2$ structure. In addition, APT reconstructions of atoms inside γ'-precipitates interconnected by a neck, in the as-quenched state, demonstrate the alternating Al-rich planes of the $L1_2$-ordered structure in both γ'-precipitates and the interconnecting necks. These results suggest that phase separation and ordering are occurring concurrently at 1073 K and during the quench to room temperature.

The partitioning behavior is quantitatively determined by calculating the partitioning ratio, $K^{\gamma'/\gamma}$, for each element, which is given by the ratio of the atomic

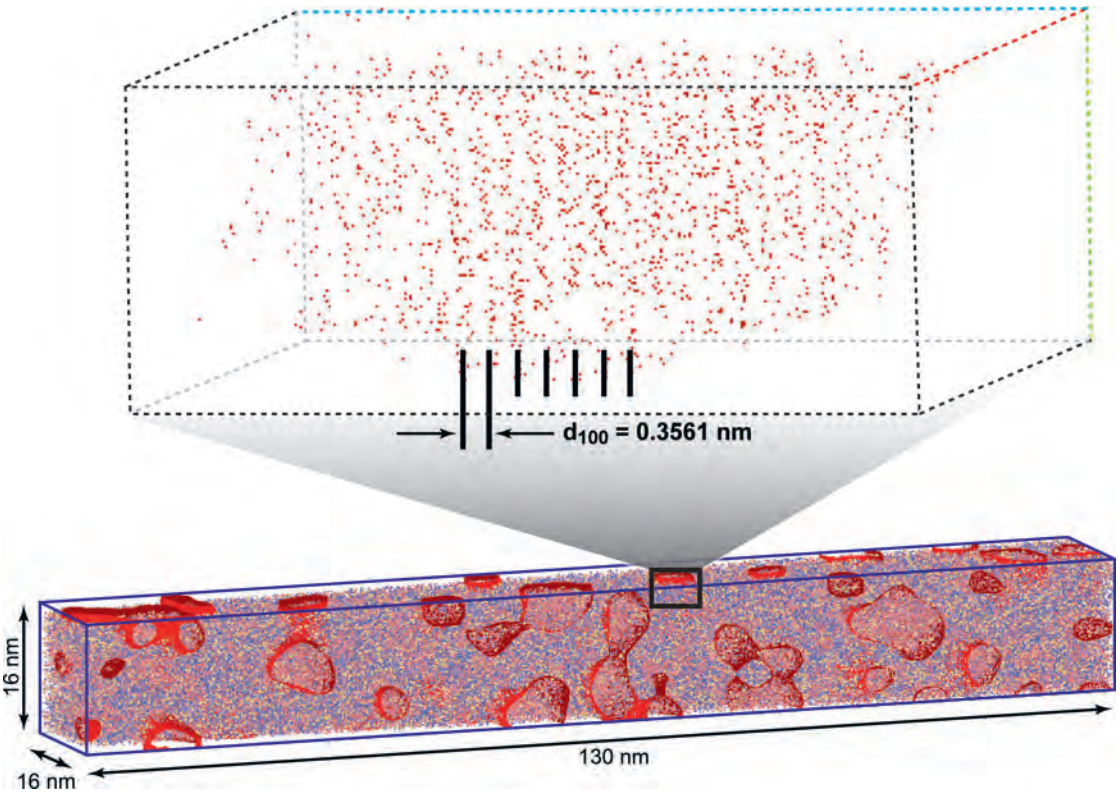

Figure 9

APT reconstruction of a Ni–10 at.% Al–8.5 at.% Cr–2 at.% Re alloy in the as-quenched state, which indicates the presence of γ′-precipitates. A 12 at.% Al isoconcentration surface is used to indicate the γ/γ′ interfaces. A portion of the γ′-precipitate is magnified, with Al (*red*), Cr (*blue*), and Re (*orange*) atoms shown to display the alternating Al planes in the [100] direction of the ordered $L1_2$ structure. Ni atoms are not shown for the sake of clarity. Adapted from Reference 129.

concentration of element *i* in γ′-precipitates divided by the atomic concentration of *i* in the γ-matrix. The values of $K^{\gamma'/\gamma}$ of the Ni–10 at.% Al–8.5 at.% Cr–2 at.% Re alloy are compared with the values of $K^{\gamma'/\gamma}$ in the ternary Ni–10 at.% Al–8.5 at.% Cr and quaternary Ni–10 at.% Al–8.5 at.% Cr–2 at.% W alloys in **Figure 11**. This figure demonstrates that the addition of Re to a Ni-Al-Cr alloy increases the partitioning of Al to γ′-precipitates and of Cr to the γ-matrix. The effect, however, of adding Re on the value of $K^{\gamma'/\gamma}$ of alloying elements is smaller than that of adding W to the same Ni-Al-Cr ternary alloy.

In conclusion, all the results presented in this section demonstrate the powerful atomic-scale resolution of APT and its contributions to unraveling kinetic pathways of a phase transformation in complex concentrated multicomponent alloys. This information is presently not obtainable by any other technique.

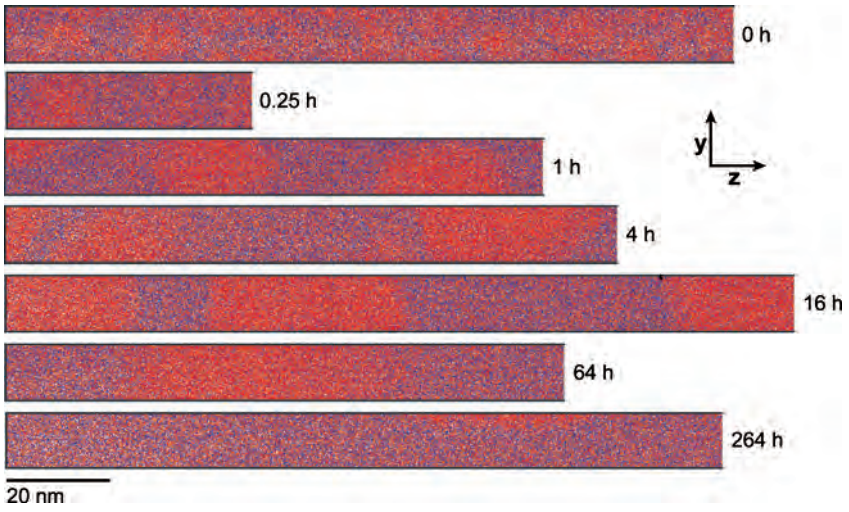

Figure 10

APT of a Ni–10 at.% Al–8.5 at.% Cr–2 at.% Re alloy at different aging times, displaying the temporal evolution of the γ′-precipitates. The cross section of each volume is perpendicular to the plane of the page. Al, Cr, and Re atoms are shown in red, blue, and orange, respectively. At 264 h only a small portion of a γ′-precipitate is detectable in this analysis volume. Adapted from Reference 129.

Three-Dimensional Nanoscale Composition Mapping of Semiconductor Wires

Semiconducting nanowires of controlled composition and doping (110–113) exhibit great promise as multifunctional components in a number of emerging device technologies (114–116). The continued advancement of these nanometer-scale devices depends critically on knowledge of their atomic-scale structures (117) because compositional fluctuations as small as a single atom can affect device performance. Thus, there is a compelling reason to determine accurate compositions of individual nanowires at the atomic scale with both high precision and accuracy. The spatial resolution of secondary ion mass spectroscopy (SIMS) (for example, NanoSIMS50, manufactured by Cameca, France) is now less than 100 nm, but the length scales of interest for nanowires are significantly smaller. HREM is capable of imaging single dopant atoms under specific conditions (119) but HREM cannot yet be considered a general tool for the 3-D mapping of dopant atoms at low concentrations in nanostructures. The critical challenge of doping atoms into the volume of nanowires and nanocrystals, although avoiding surface segregation, emphasizes the compelling need for 3-D composition characterization of these nanostructures. In this section we present LEAP™ tomographic results on the positions of single Au atoms in an InAs nanowire and imaging of the heterophase interface between a Au catalyst and the InAs nanowire in 3-D with 0.3-nm resolution. These results help to establish APT as a uniquely powerful instrument for analyzing the chemical compositions of semiconductor nanostructures.

Functional 1-D semiconductor nanostructures have been synthesized by a number of methods. In the research presented herein, electron-beam lithography followed by metal evaporation and lift-off were used to pattern an array of Au catalyst disks on a GaAs(111)B wafer. The Au seeds catalyzed the growth of InAs nanowires in a quartz metal-organic vapor-phase epitaxy (MOVPE) reactor with

Figure 11

Partitioning ratio of all the elements in (*a*) Ni–10 at.% Al–8.5 at.% Cr, (*b*) Ni–10 at.% Al–8.5 at.% Cr–2 at.% W, and (*c*) Ni–10 at.% Al–8.5 at.% Cr–2 at.% Re alloy plotted as a function of aging time. This graph displays the effect of the Re addition on the partitioning behavior of all alloying elements in a Ni-based model superalloy. Adapted from Reference 129.

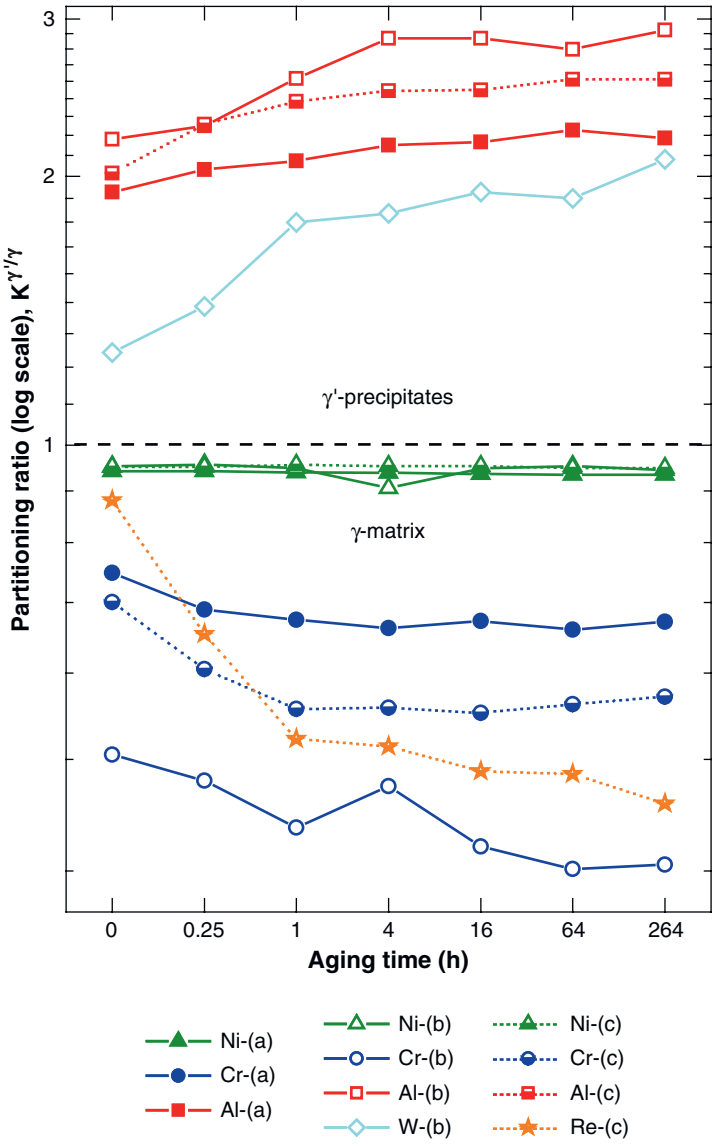

trimethylindium and arsine as reactant chemical precursors and hydrogen as the carrier gas under conditions described elsewhere (120). In this manner, arrays of epitaxial vertically oriented InAs nanowires 100–140 μm long and spaced 500 μm apart were generated, which facilitated the LEAP™ tomographic analysis (see left panel in **Figure 2**).

Figure 12 presents a 3-D reconstruction of an InAs nanowire generated from a data set of 1.3×10^6 atoms pulsed field evaporated sequentially in the LEAP™ tomograph (121). The side view of **Figure 12*a*** shows that analysis volumes comparable

to an entire nanowire-based device, such as the channel of a nanowire transistor (122), are well within the capabilities of this technique. When looking along the nanowire's axis (**Figure 12*b***), one clearly observes hexagonal facets, and comparison with an SEM image (**Figure 12*c***) verifies that we have accurately reconstructed the nanowire's cross section. [Although TEM observations reveal a thin (1–2 nm) amorphous oxide layer on InAs nanowires, we do not see oxygen-related peaks in the TOF mass spectra. We think that the oxygen species are evaporating between voltage pulses, and this issue should be resolved in the future using the picosecond laser.] More significantly, a magnified view perpendicular to the nanowire reveals distinct planes of atoms extending across the nanowires (**Figure 12*d***). These atomic planes lie perpendicular to the wurtzite [0001] growth direction at a spacing of 0.35 nm, as determined by TEM, and therefore the observation of atomic planes by LEAP™ tomography demonstrates subnanometer resolution.

SEM: scanning electron microscope

Although **Figure 12** presents useful 2-D projections, the 3-D position and chemical identity of every atom are retained in the original data set, which is not generally the case for TEM observations. To emphasize this point, **Figure 12*e*** presents an enlarged section of the nanowire shown in **Figure 12*a***, using spheres to represent each individual Au atom found within the analyzed volume. **Figure 12*a*** makes clear that dopant concentrations and fluctuations can be extracted by averaging over a chosen volume. From this figure, we can immediately draw two conclusions. First, one can determine whether the catalyst employed in nanowire growth schemes becomes incorporated in the bulk of the nanowires. This question is of critical importance to the performance of nanowire devices because metal atoms, such as Au, can strongly influence electronic properties. Second, LEAP™ tomography can be used to reveal the concentrations and distributions of dopants in a range of chemically synthesized nanostructures (123) and may therefore play a critical role in addressing the major challenge of dopant incorporation and segregation in nanomaterials.

Another important capability of the LEAP™ tomograph is the imaging of interfaces within a nanostructure, because functional heterointerfaces form the basis of most semiconductor devices (124). In particular, one would like to be able to analyze the compositional abruptness of junctions within nanowires without averaging over the nanowire diameter. **Figure 13** displays an analysis of a reconstructed nanowire section including a Au catalyst/InAs nanowire heterophase interface. As anticipated, the Au catalyst lies atop the nanowires during and after growth. The four "slices" of **Figure 13*a***, two on either side of the interface, demonstrate that tomographic analyses can reveal both radial and axial composition variations within a nanowire. Although the catalyst/nanowire heterophase interface appears qualitatively abrupt in **Figure 13*b***, the interface width is more readily ascertained by plotting a 1-D composition profile derived from a cylindrical cross section perpendicular to the interface (**Figure 13*c***); the interface between the catalyst ($Au_{0.9}In_{0.1}$) is abrupt, with a width of less than 0.5 nm. Because nanowire growth occurs at this heterophase interface, its structure may influence the widths of intrawire semiconductor growth processes, particularly the metal-catalyzed VLS growth process (125).

This 3-D composition mapping of a semiconductor nanowire, with subnanometer resolution, establishes that LEAP™ tomography can play an important role in the

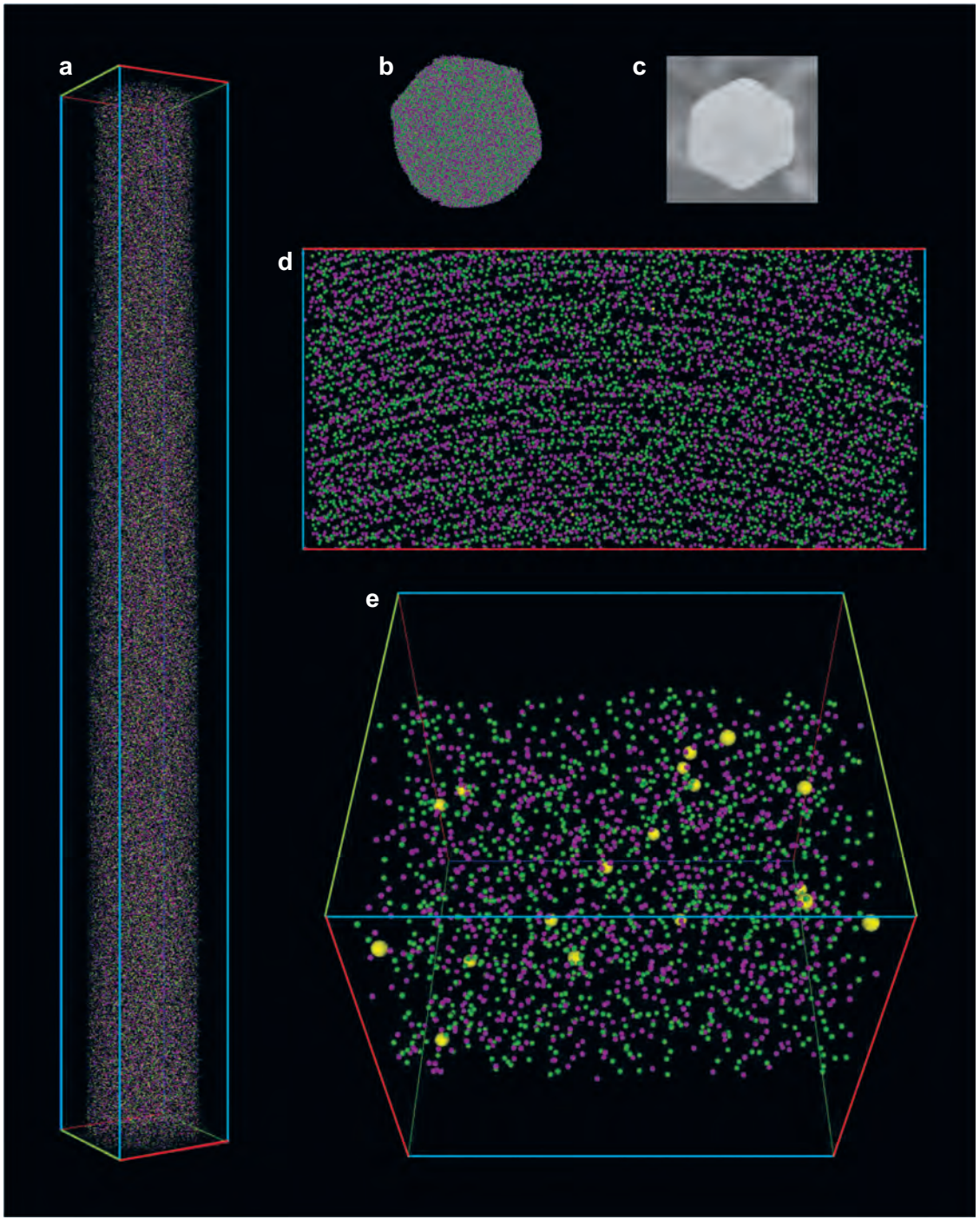

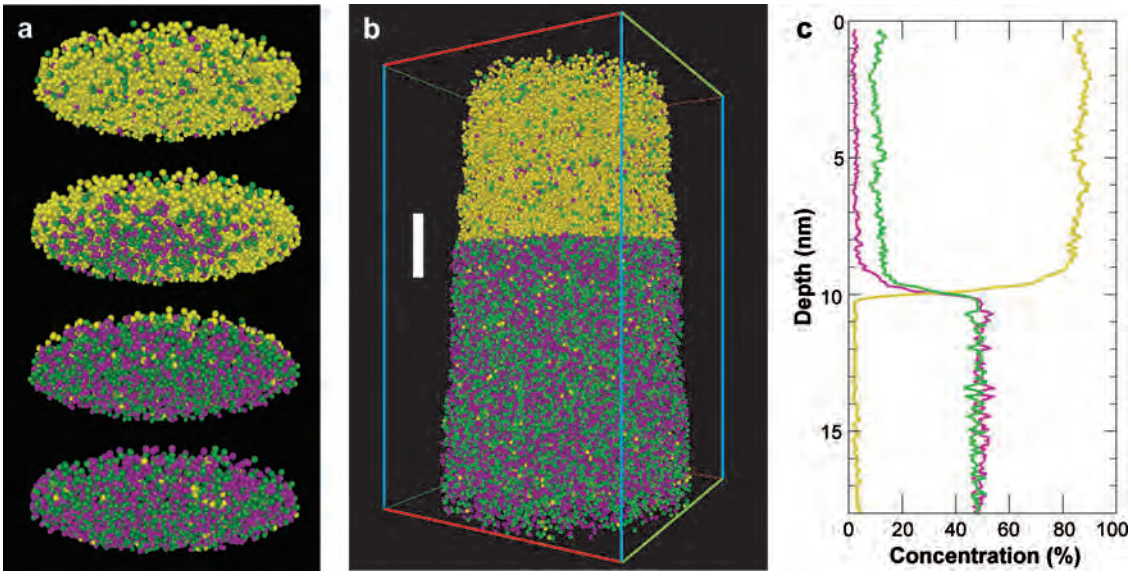

Figure 13

Catalyst nanowires interface in 3-D. (*a*) One-nm-thick slices through the nanowires over the region defined by the white bar in *b*. The diameter of the slices is 10 nm. In, As, and Au atoms are rendered as green, purple, and yellow dots, respectively. (*b*) A $14 \times 14 \times 23$ nm^3 reconstruction of an InAs nanowire tip showing a Au catalyst particle at the top. (*c*) Composition profile in 1-D plotted along the growth axis and through the catalyst/nanowire interface. The plotted composition is a radially average value within a 4-nm-diameter cylinder centered in the middle of the nanowire. From Reference 121.

development of semiconductor nanostructure device technology by providing critical insights into the connection between synthesis schemes and nanoscale composition. LEAP^{TM} tomography has the potential to be applied to other semiconductor nanostructures, including nanocrystals, by depositing samples on arrays of posts elevated

Figure 12

Three-dimensional reconstruction of an InAs nanowire. The sample temperature was at a fixed value between 50 K to 100 K, and the ambient pressure in the LEAP^{TM} tomograph was 10^{-10} Torr during its atom-by-atom dissection. (*a*) Side view (perpendicular to growth axis) of a $25 \times 25 \times 300$ nm^3 reconstruction of the nanowire. In, As, and Au atoms are rendered as green, purple, and yellow dots, respectively. Only 5% of the atoms are displayed to provide a sense of depth. (*b*) A 21×21 nm^2 end-on view of nanowire reconstruction showing hexagonal faceting. (*c*) SEM micrograph of an InAs nanowire displaying a hexagonal cross section (1.7 μm^2). (*d*) Magnified side view of the nanowire displaying (0001) atomic planes. The dimensions are 23×14 nm^2. The slight curvature of the atomic planes is an artifact; the software used for the reconstruction assumes a hemispherical end-form for the field-evaporating nanowires. (*e*) For clarity, a $27 \times 27 \times 29$ nm^3 reconstruction of the nanowire with Au atoms is enlarged, and 2% of In and As atoms are shown; the growth axis runs left to right. The 18 Au atoms within the volume correspond to a concentration of 100 atomic parts per million. From Reference 121.

from the substrate (126). Additionally, given the concurrent development of nanoscale property measurements via scanned probes (127), LEAP^{TM} tomography promises to advance materials science by extending our understanding of structure-property relationships to the nanoscale limit.

CONCLUSIONS

The commercialization of APTs—which are well designed, sophisticated, ergonomic, and computer controlled and involve powerful software for analyzing the data collected—is resulting in a revolutionary phase in the development and application of this experimental instrument to problems in materials science and engineering that cannot be solved using other instruments. In this review we provide proof of this conclusion by presenting results (see section on Applications) for the following three problems that yield unique and quantitative information: (*a*) the segregation of Mg at coherent α-Al/Al_3Sc heterophase interfaces, (*b*) the determination of the kinetic pathways for the decomposition of ternary Ni-Al-Cr and quaternary Ni-Al-Cr-Re alloys, and (*c*) 3-D nanoscale composition mapping of InAs nanowires grown by the VLS technique.

SUMMARY POINTS

1. An APT consists of an FIM plus a special TOF mass spectrometer with a 2-D position-sensitive detector. The TOF of an ion yields its chemical identity, whereas the position-sensitive detector gives its x- and y-coordinates in an {hkl} plane. This information permits one to reconstruct a crystal lattice in 3-D.
2. A LEAP^{TM} tomograph employing a picosecond laser, with a pulse repetition rate of 500 kHz, permits one to collect and analyze up to 300×10^6 ion h^{-1}. This implies that it is now possible to measure concentrations of atoms at the level of one atomic part per million that are statistically significant.
3. We have measured the Gibbsian interfacial excess of Mg at a coherent α-Al/Al_3Sc heterophase interface in an Al-Sc-Mg alloy and demonstrated that this is the thermodynamic equilibrium value. Additionally, first-principles theory has shown that the driving force for segregation of Mg is electronic (chemical) and not the elastic strain energy associated with the oversized Mg atom.
4. The kinetic pathways for nucleation, growth, and coarsening of Ni_3 ($Al_{1-x}Cr_x$) ($L1_2$) γ'-precipitates in a Ni-Al-Cr ternary alloy have been measured in quantitative detail using APT. Such pathways show that the composition of $Ni_3(Al_{1-x}Cr_x)$ precipitates, which are not along the tie line connecting the γ- and γ'-phases, evolves temporally toward its equilibrium value.
5. The role of Re regarding the kinetic pathways for nucleation, growth, and coarsening in a Ni-Al-Cr-Re quaternary alloy has been determined

employing APT. Details on how the partitioning ratios of Al, Cr, and Re change temporally for the γ-matrix and γ'-precipitates are presented. Additionally, partitioning of the elements in a Ni-Al-Cr alloy is compared with partitioning of the elements in the Ni-Al-Cr-Re alloy.

6. The compositions of an InAs nanowire grown by the VLS technique, where the catalyst is Au, were measured using LEAP™ tomography. From these measurements, the Au solubility in InAs was determined, and the concentrations of In and As in the Au catalyst were extracted from the experimental data.

ACKNOWLEDGMENTS

Atom-probe tomographic measurements were performed at the Northwestern University Center for Atom-Probe Tomography (NUCAPT: **http://nucapt.northwestern.edu**). The LEAP™ tomograph was purchased with funding from the NSF-MRI (DMR 0420532) and ONR-DURIP (N00014-0400798) (Julie Christodoulou, grant officer, programs). Additionally, the LEAP™ tomograph was enhanced in May 2006 with a picosecond laser with funding from the ONR-DURIP (N0014-06-1-0539) program (Julie Christodoulou, grant officer). The research on model Ni-based superalloys was supported by the National Science Foundation, Division of Materials Research, under contract DMR-0241928. The research on Al-Sc-Mg alloys was supported by the Department of Energy. The research on InAs nanowires was supported by the Office of Naval Research (L.J.L., N00014-05-1-0566), Northwestern University, a National Science Foundation through CAREER (L.J.L., DMR-0449933), and MRSEC seed funding (L.J.L.). The following colleagues are thanked for their critical help to make this short review possible: Mark D. Asta, David C. Dunand, Lincoln J. Lauhon, Emmanuelle A. Marquis, Daniel E. Perea, Chantal K. Sudbrack, and Kevin E. Yoon. Dieter Isheim is kindly thanked for his enthusiastic help with APT, managing NUCAPT, and discussions.

LITERATURE CITED

1. Jacoby M. 2005. Atomic imaging turns 50. *Chem. Eng. News* 83(48):13–16
2. Müller EW. 1951. The field ion microscope. *Z. Physik* 131:136–42
3. Müller EW. 1953. Feldemission. *Ergeb. Exakten Naturwiss.* 27:290–360
4. Müller EW, Tsong TT. 1969. *Field Ion Microscopy*. New York: American Elsevier
5. Oppenheimer JR. 1928. Three notes on the quantum theory of aperiodic effects. *Phys. Rev.* 31:66–81
6. Inghram MG, Gomer R. 1954. Mass spectrometric analysis of ions from the field ion microscope. *J. Chem. Phys.* 22:1279–80
7. Inghram MG, Gomer R. 1955. Massenspektrometrische untersuchungen der feldemission positiver ionen. *Z. Naturforsch.* 10a:863–72
8. Tsong TT, Müller EW. 1965. Measurement of the energy distributions in field ionization. *J. Chem. Phys.* 41:3279–84

9. Müller EW, Bahadur K. 1956. Field ionization of gases at a metal surface and the resolution of the field ion microscope. *Phys. Rev*. 102:624–31
10. Gomer R. 1961. *Field Emission and Field Ionization*. Cambridge, MA: Harvard Univ. Press
11. Chen YC, Seidman DN. 1971. The field ionization characteristics of individual atomic planes. *Surf. Sci.* 27:231–55
12. Kasner E, Newman J. 1940. *Mathematics and the Imagination*. New York: Simon & Schuster
13. Chen YC, Seidman DN. 1971. On the atomic resolution of a field-ion microscope. *Surf. Sci.* 26:61–84
14. Müller EW. 1956. Field desorption. *Phys. Rev*. 102:618–24
15. Gomer R. 1959. Field desorption. *J. Chem. Phys*. 31:341–45
16. Gomer R, Swanson LW. 1963. Theory of field desorption. *J. Chem. Phys*. 38:1613–29
17. Brandon DG. 1965. Structure of field-evaporated surfaces. *Surf. Sci*. 3:1–18
18. Tsong TT. 1990. *Atom-Probe Field-Ion Microscopy*. Cambridge, UK: Cambridge Univ. Press

19, 20. First quantitative direct observations of mono- and divacancies that are not artifacts. Results are used to explain diffusion in Pt.

19. Berger AS, Seidman DN, Balluffi RW. 1973. A quantitative study of vacancy defects in quenched platinum by field-ion microscopy and electrical resistivity measurements. I. Experimental results. *Acta Metall*. 21:123–35

20. Berger AS, Seidman DN, Balluffi RW. 1973. A quantitative study of vacancy defects in quenched platinum by field-ion microscopy and electrical resistivity measurements. II. Analysis. *Acta Metall*. 21:136–47

21, 22, 23. First direct quantitative FIM measurements of uncorrelated migration of self-interstitial atoms produced by in situ heavy ion irradiation.

21. Scanlan RM, Styris DL, Seidman DN. 1971. An in situ field-ion microscope study of irradiated tungsten. I. Experimental results. *Philos. Mag*. 23:1439–57

22. Scanlan RM, Styris DL, Seidman DN. 1971. An in situ field-ion microscope study of irradiated tungsten. II. Analysis and interpretation. *Philos. Mag*. 23:1459–78

23. Petroff P, Seidman DN. 1971. Direct observation of long-range migration of self-interstitial atoms in stage I of irradiated platinum. *Appl. Phys. Lett*. 18:518–20

24. Bowkett KM, Smith DA. 1970. *Field-Ion Microscopy: Defects in Crystalline Solids*. Amsterdam: North-Holland
25. Seidman DN, Burke JJ. 1974. Field-ion microscope observations of the threefold symmetric dissociation of ⟨111⟩ screw dislocations in molybdenum. *Acta Metall*. 22:1301–14

26, 27. First direct quantitative measurements by APFIM of solute segregation at stacking faults (a 2-D imperfection).

26. Herschitz R, Seidman DN. 1985. Atomic resolution observations of solute-atom segregation effects and phase transitions in stacking faults in dilute cobalt alloys. I. Experimental results. *Acta Metall*. 33:1547–63

27. Herschitz R, Seidman DN. 1985. Atomic resolution observations of solute-atom segregation effects and phase transitions in stacking faults in dilute cobalt alloys. II. Analysis and discussion. *Acta Metall*. 33:1565–76

28. Hren JJ, Ranganathan S, ed. 1968. *Field-Ion Microscopy*. New York: Plenum Press
29. Seidman DN. 1973. The direct observation of point defects in irradiated or quenched metals by quantitative field-ion microscopy. *J. Phys. F* 3:393–421
30. Seidman DN. 1976. Field-ion microscope studies of the defect structure of the primary state of radiation damage of irradiated metals. In *Radiation Damage in Metals*, ed. NL Peterson, SD Harkness, pp. 28–57. Metals Park, OH: Am. Soc. Metals
31. Seidman DN. 1978. Study of radiation-damage in metals with field-ion and atom-probe microscopes. *Surf. Sci.* 70:532–65
32. Pramanik D, Seidman DN. 1986. Atomic resolution study of displacement cascades in ion-irradiated platinum. *J. Appl. Phys.* 60:137–50
33. Seidman DN, Averback RS, Benedek R. 1987. Displacement cascades: dynamics and atomic structure. *Phys. Status Solidi B* 144:85–104
34. Ehrlich G, Hudda FG. 1961. Low-temperature chemisorption: studies in a field emission microscope. *J. Chem. Phys*. 35:1421–39
35. Ehrlich G, Hudda FG. 1966. Atomic view of surface self-diffusion: tungsten on tungsten. *J. Chem. Phys*. 44:1039–49
36. Ehrlich G. 1980. Quantitative examination of individual atomic events on solids. *J. Vac. Sci. Tech*. 17:9–14
37. Tsong TT. 1980. Quantitative investigations of atomic processes on metal-surfaces at atomic resolution. *Prog. Surf. Sci*. 10:165–248
38. Müller EW, Tsong TT. 1973. Field ion microscopy, field ionization, field evaporation. *Prog. Surf. Sci*. 4(1):1–139
39. Müller EW, Panitz JA, McLane SB. 1968. Atom-probe field ion microscope. *Rev. Sci. Instum*. 39:83–86
40. Wagner A, Hall TM, Seidman DN. 1975. A simplified method for the calibration of an atom probe field-ion microscope. *Rev. Sci. Instrum*. 46:1032–34
41. Hall TM, Wagner A, Berger AS, Seidman DN. 1976. An atom-probe field-ion microscope for the study of defects in metals. *Scripta Metall*. 10:485–88
42. Hall TM, Wagner A, Seidman. 1977. A computer controlled time-of-flight atom-probe field-ion microscope for the study of defects in metals. *J. Phys. E* 10:884–93
43. Wagner A, Hall TM, Seidman DN. 1978. An atom-probe field-ion microscope for the study of the interaction of impurity atoms or alloying elements with defects. *J. Nuclear Mater.* 69–70:413–23
44. Wagner R. 1982. *Field-Ion Microscopy*. Berlin: Springer-Verlag
45. Herschitz R, Seidman DN. 1984. An atomic resolution study of homogenous radiation-induced precipitation in a neutron-irradiated W-10 at. % Re alloy. *Acta Metall.* 32:1141–54
46. Herschitz R, Seidman DN. 1984. An atomic resolution study of radiation-induced precipitation and solute segregation effects in a neutron-irradiated W-25 at.% Re alloy. *Acta Metall.* 32:1155–71

29–31. Review articles of fundamental studies of point defects (vacancies and self-interstitial atoms) by FIM in quenched or irradiated metals.

32, 33. Point-defect structure(s) of displacement cascades in irradiated metals by FIM, with an emphasis on obtaining fundamental and quantitative information.

45, 46. APFIM studies of homogeneous radiation-induced precipitation, which provide direct evidence for the chemical changes associated with this phenomenon.

47. Sakurai T, Sakai A, Pickering HW. 1989. *Atom-Probe Field Ion Microscopy and Its Applications*. Boston: Academic
48. Miller MK, Smith GDW. 1989. *Atom Probe Microanalysis: Principles and Applications to Materials Problems*. Pittsburgh: Mater. Res. Soc.
49. Miller MK, Cerezo A, Hetherington MG, Smith GDW. 1996. *Atom Probe Field Ion Microscopy*. Oxford, UK: Oxford Sci. Publ.
50. Panitz JA. 1973. 10 cm atom probe. *Rev. Sci. Instrum*. 44:1034–38
51. Panitz JA. 1975. *U.S. Patent No. 3,868,507*
52. Kellogg GL. 1987. Ion signal calibration in the imaging atom-probe with an external, time-gated image intensifier. *Rev. Sci. Instrum*. 58:38–42
53. Cerezo A, Godfrey TJ, Smith GDW. 1988. Application of a position-sensitive detector to atom probe microanalysis. *Rev. Sci. Instrum*. 59:862–66
54. Blavette D. Deconihut B, Bostel A, Sarru JM, Bouet M, Menand A. 1993. The tomographic atom-probe: a quantitative 3-dimensional nanoanalytical instrument on an atomic-scale. *Rev. Sci. Instrum*. 64:2911–19
55. Cerezo A, Godfrey TJ, Hyde JM, Sijbrandij SJ, Smith GDW. 1994. Improvements in 3-dimensional atom-probe design. *Appl. Surf. Sci.* 76/77:374–81
56. Miller MK. 2000. *Atom Probe Tomography: Analysis at the Atomic Level*. New York: Kluwer/Plenum

57, 58. APFIM studies of the range profiles and migration of low-energy implanted $^3He^+$ and $^4He^+$ in tungsten at cryogenic temperatures.

57. Amano J, Wagner A, Seidman DN. 1981. Range profiles of low-energy (100 to 1500 eV) implanted ^{3}He and ^{4}He atoms in tungsten. I. Experimental results. *Philos. Mag. A*. 44:177–98

58. Amano J, Wagner A, Seidman DN. 1981. Range profiles of low-energy (100 to 1500 eV) implanted ^{3}He and ^{4}He atoms in tungsten. II. Analysis and interpretation. *Philos. Mag. A* 44:199–222

59. Amano J, Seidman DN. 1981. Experimental determination of the particle reflection coefficients of low-energy (100 to 1000 eV) ^{3}He atoms from the (110) plane of tungsten. *J. Appl. Phys*. 52:6934–38
60. Macrander AT, Seidman DN. 1984. An atom-probe field-ion microscope study of 200 eV H_2^+ ions implanted in tungsten at 29 K. *J. Appl. Phys*. 56:1623–29
61. Kelly TF, Camus PP, Larson DJ, Holzman LM, Bajikav SS. 1996. On the many advantages of local-electrode atom probes. *Ultramicroscopy* 62:29–42
62. Nishikawa O, Kimoto M. 1994. Toward a scanning atom-probe: computer-simulation of electric-field. *Appl. Surf. Sci.* 76(1–4):424–30
63. Gault B, Vurpillot F, Bostel A, Menand A, Deconihut B. 2005. Estimation of the tip field enhancement on a field emitter under laser illumination. *Appl. Phys. Lett*. 86:094101/1–3
64. Cerezo A, Smith GDW, Clifton PH. 2006. Measurement of temperature rises in the femtosecond laser pulsed three-dimensional atom probe. *Appl. Phys. Lett*. 88:154103/1–3
65. Scheinfein MR, Seidman DN. 1993. Time aberrations of uniform fields: an improved reflectron mass spectrometer for an atom-probe field-ion microscope. *Rev. Sci. Instrum*. 64:3126–31
66. Gorelikov DV. 2001. *A high resolution pulsed-laser atom-probefield-ion microscope*. PhD thesis. Northwestern Univ. 179 pp.

67. Toropova LS, Eskin DG, Kharakterova ML, Dobatkina TV. 1998. *Advanced Aluminum Alloys Containing Scandium*. Amsterdam: Gordon & Breach
68. Marquis EA, Seidman DN. 2001. Nanoscale morphological evolution of Al_3Sc precipitates in Al(Sc) alloys. *Acta Mater*. 49:1909–19
69. Marquis EA. 2002. *Microstructural evolution and strengthening mechanisms in Al-Sc and Al-Mg-Sc alloys*. PhD thesis. Northwestern Univ. 245 pp.
70. Hellman OC, Vandenbroucke, Rüsing J, Isheim D, Seidman DN. 2000. Analysis of three-dimensional atom-probe data by the proximity histogram. *Micros. Microanal*. 6:437–44
71. Jo HH, Fujikawa SI. 1993. Kinetics of precipitation in Al-Sc alloys and low-temperature solid solubility of scandium in aluminum studied by electrical-resistivity measurements. *Mater. Sci. Eng. A* 171:151–61
72. Novotny GM, Ardell AJ. 2001. Precipitation of Al_3Sc in binary Al-Sc alloys. *Mater. Sci. Eng. A* 318:144–54
73. Kuehmann CJ, Voorhees PW. 1996. Ostwald ripening in ternary alloys. *Metall. Mater. Trans. A* 27:937–43
74. Ozoliņš V, Asta MD. 2001. Large vibrational effects upon calculated phase boundaries in Al-Sc. *Phys. Rev. Lett*. 86:448–51
75. Asta M, Ozoliņš V. 2001. Structural, vibrational, and thermodynamic properties of Al-Sc alloys and intermetallic compounds. *Phys. Rev. B* 64:094104/1–14
76. Woodward C, Asta M, Kresse G, Hafner J. 2001. Density of constitutional and thermal point defects in $L1_2$ Al_3Sc. *Phys. Rev. B* 63:094103/1–6
77. Fujikawa SI. 1997. Impurity diffusion of scandium in aluminum. *Defect Diff. Forum*. 143:115–20
78. Rothman SJ, Peterson NL, Nowicki LJ, Robinson LC. 1974. Tracer diffusion of magnesium in aluminum single-crystals. *Phys. Status Solidi B* 63:K29–33
79. Asta M, Foiles SM, Quong AA. 1998. First-principles calculations of bulk and interfacial thermodynamic properties for fcc-based Al-Sc alloys. *Phys. Rev. B* 57:11265–75
80. Dregia SA, Wynblatt P. 1991. Equilibrium segregation and interfacial energy in multicomponent systems. *Acta Metall. Mater*. 39:771–78
81. Krakauer BW, Seidman DN. 1993. Absolute atomic scale measurements of the Gibbsian interfacial excess of solute at internal interfaces. *Phys. Rev. B* 48:6724–27
82. Krakauer BW, Seidman DN. 1998. Subnanometer scale study of segregation at grain boundaries in an Fe (Si) alloy. *Acta Mater*. 46:6145–61
83. Seidman DN, Krakauer BW, Udler D. 1994. Atomic scale studies of solute-atom segregation at grain boundaries: experiments and simulations. *J. Phys. Chem. Solids* 55:1035–57
84. Marquis EA, Seidman DN. 2004. Nanostructural evolution of $Al3_3Sc$ precipitates in an Al-Sc-Mg alloy by three-dimensional atom-probe microscopy. *Surf. Interf. Anal*. 36:559–63
85. Marquis EA, Seidman DN. 2005. The temporal evolution of Al_3Sc precipitates on a nanoscale in an Al-Mg-Sc alloy. *Acta Mater*. 53:4259–68

81–83. Direct determination of the Gibbsian interfacial excess of a solute atom at an internal interface without data deconvolution by APFIM.

84, 85. First direct measurements of Gibbsian interfacial excess of solute atoms at a coherent heterophase interfaces, APT experiments, and theory.

86. Marquis EA, Seidman DN, Asta M, Woodward CM, Ozoliņš V. 2003. Segregation at Al/Al_3Sc heterophase interfaces on an atomic scale: experiments and computations. *Phys. Rev. Lett*. 91:036101/1–4
87. Marquis EA, Seidman DN, Asta M, Woodward CM. 2006. Effects of Mg on the nanostructural temporal evolution of Al_3Sc precipitates: experiments and simulation. *Acta Mater*. 54:119–30
88. Sudbrack CK, Yoon KE, Mao Z, Noebe RD, Isheim D, Seidman. 2003. Temporal evolution of nanostructures in a model nickel-base superalloy: experiments and simulations. In *Electron Microscopy: Its Role in Materials Research—The Mike Meshii Symposium*. ed. JR Weertman, ME Fine, KT Faber, W King, P Liaw, pp. 43–50. Warrendale, PA: Miner. Met. Mater. Soc.
89. Sudbrack CK, Noebe RD, Seidman DN. 2005. Temporal evolution of subnanometer compositional profiles across the γ/γ' interface in a model Ni-Al-Cr superalloy. In *Solid-Solid Phase Transformations in Inorganic Materials*, ed. JM Howe, DE Laughlin, JK Lee, U Dahmen, WA Soffa, 2:543–48. Warrendale, PA: Miner. Met. Mater. Soc.
90. Yoon KE, Sudbrack CK, Noebe RD, Seidman. 2005. The temporal evolution of the nanostructures of model Ni-Al-Cr and Ni-Al-Cr-Re superalloys. *Z. Metall.* 96:481–85
91. Sudbrack CK, Yoon KE, Noebe RD, Seidman DN. 2006. Temporal evolution of the nanostructure and phase compositions in a model Ni-Al-Cr superalloy. *Acta Mater*. 54:3199–210
92. Sudbrack CK, Noebe RD, Seidman DN. 2006. Direct observations of nucleation in a nondilute multicomponent alloy. *Phys. Rev. B* 73:212101/1–4
93. Sudbrack CK, Noebe RD, Seidman DN. 2007. Compositional pathways and capillary effects during isothermal precipitation in a nondilute Ni-Al-Cr superalloy. *Acta Mater*. 55:119–30
94. Wendt H, Haasen P. 1983. Nucleation and growth of γ'-precipitates in Ni-14 atomic percent Al. *Acta Metall.* 31:1649–59
95. Xiao SQ, Haasen P. 1991. HREM investigation of homogeneous decomposition in a Ni-12 atomic percent Al alloy. *Acta Metall.* 39:651–59
96. Wanderka N, Glatzel U. 1995. Chemical composition measurements of a nickel-base superalloy by atom probe field ion microscopy. *Mater. Sci. Eng. A* 203:69–74
97. Staron P, Kampmann R. 2000. Early-stage decomposition kinetics in Ni-Al alloys. I. Small and wide-angle neutron scattering investigation on Ni-13 at.% Al and cluster dynamics modeling. *Acta Mater*. 48:701–12
98. Schmuck C, Caron P, Hauet A, Blavette D. 1997. Ordering and precipitation of γ'-phase in low supersaturated Ni-Cr-Al model alloy: an atomic scale investigation. *Philos. Mag. A* 76:527–42
99. Pareige C, Soisson F, Martin G, Blavette D. 1999. Ordering and phase separation in Ni-Cr-Al: Monte Carlo simulations vs. three-dimensional atom probe. *Acta Mater*. 47:1889–99
100. Sudbrack CK. 2004. *Decompositional behavior in model Ni-Al-Cr-X superalloys: temporal evolution and compositional pathways on a nanoscale*. PhD thesis. Northwestern Univ. 209 pp.

92. Direct observations of the chemical pathways that lead to nucleation in a concentrated multicomponent alloy.

93. First direct measurement of excess solute supersaturations in γ'-precipitates resulting from capillary effects (Gibbs-Thomson effect).

101. Yoon KE. 2004. *Temporal evolution of the chemistry and nanostructure of multicomponent model Ni-based superalloys*. PhD thesis. Northwestern Univ. 189 pp.
102. Umantsev A, Olson GB. 1993. Ostwald ripening in multicomponent alloys. *Scripta Metall.* 29:1135–40
103. Kuehmann CJ, Voorhees PW. 1996. Ostwald ripening in ternary alloys. *Metall. Mater. Trans.* 27A:937–43
104. Yoon KE, Noebe RD, Seidman DN. 2007. Effects of a rhenium addition on the temporal evolution of the nanostructure and chemistry of a model Ni-Cr-Al superalloy. I. Experimental observations. *Acta Mater.* 55:1145–57
105. Yoon KE, Noebe RD, Seidman DN. 2007. Effects of a rhenium addition on the temporal evolution of the nanostructure and chemistry of a model Ni-Cr-Al superalloy. II. Analysis of the coarsening behavior. *Acta Mater.* 55:1159–69
106. Anton DL, Lemkey FD. 1984. Quinary alloy modifications of the eutectic superalloy $\gamma/\gamma'+Cr_3C_2$. In *Fifth International Symposium on Superalloys*, ed. M Gell, CS Kortovich, RH Bricknell, WB Kent, JF Radavich, pp. 601–10. Champion, PA: AIME
107. Giamei AF, Anton DL. 1985. Rhenium additions to a Ni-Base superalloy: effects of microstructure. *Met. Trans. A* 16:1997–2005
108. Sudbrack CK, Isheim D, Noebe RD, Jacobson NS, Seidman DN. 2004. The influence of tungsten on the chemical composition of a temporally evolving nanostructure of a model Ni-Al-Cr superalloy. *Micros. Microanal.* 10:355–65
109. Isheim D, Hseih G, Noebe RD, Seidman DN. 2005. Nanostructural temporal evolution and solute partitioning in model Ni-based superalloys containing ruthenium, rhenium and tungsten. In *Solid-Solid Phase Transformations in Inorganic Materials 2005*, 2:309–14. ed. JM Howe, DE Laughlin, JK Lee, U Dahmen, WA Soffa. Warrendale, PA: Miner. Met. Mater. Soc.
110. Gudiksen MS, Lauhon LJ, Wang J, Smith DC, Lieber CM. 2002. Growth of nanowire superlattice structures for nanoscale photonics and electronics. *Nature* 415:617–20
111. Lauhon LJ, Gudiksen MS, Wang CL, Lieber CM. 2002. Epitaxial core-shell and core-multishell nanowire heterostructures. *Nature* 420:57–61
112. Björk MT, Ohlsson BJ, Sass T, Persson AI, Thelander C, et al. 2002. One-dimensional heterostructures in semiconductor nanowhiskers. *App. Phys. Lett.* 80:1058–60
113. Wu YY, Fan R, Yang PD. 2002. Block-by-block growth of single-crystalline Si/SiGe superlattice nanowires. *Nano Lett.* 2:83–86
114. Cui Y, Lieber CM. 2001. Functional nanoscale electronic devices assembled using silicon nanowire building blocks. *Science* 291:851–53
115. Huang Y, Duan X, Cui Y, Lauhon LJ, Kim K-H, Lieber CM. 2001. Logic gates and computation from assembled nanowire building blocks. *Science* 294:1313–17
116. Duan XF, Huang Y, Agarwal R, Lieber CM. 2003. Single-nanowire electrically driven lasers. *Nature* 421:241–45
117. Castel MR, Muller DA, Voyles PM. 2003. Dopant mapping for the nanotechnology age. *Nat. Mater.* 2:129–31

118. Deleted in proof
119. Voyles PM, Muller DA, Grazul JL, Citrin PH, Gossmann HJL. 2002. Atomic-scale imaging of individual dopant atoms and clusters in highly *n*-type bulk Si. *Nature* 416:826–29
120. May SJ, Zheng JG, Wessels BW, Lauhon LJ. 2005. Dendritic nanowire growth mediated by a self-assembled catalyst. *Adv. Mater*. 17:598–602
121. Perea DE, Allen JE, May SJ, Wessels BW, Seidman DN, Lauhon LJ. 2006. Three-dimensional nanoscale composition mapping of semiconductor nanowires. *Nano Lett*. 6(6):181–85
122. Greytak AB, Lauhon LJ, Gudiksen MS, Lieber CM. 2004. Growth and transport properties of complementary germanium nanowire field-effect transistors. *App. Phys. Lett*. 84:4176–78
123. Xia YN, Yang P, Sun Y, Wu Y, Mayers B, et al. 2003. One-dimensional nanostructures: synthesis, characterization, and applications. *Adv. Mater.* 15:353–89
124. Sze SM. 1981. *Physics of Semiconductor Devices*. New York: Wiley
125. Wagner RS. 1970. VLS mechanism of crystal growth. In *Whisker Technology*, ed. AP Levitt. pp. 47–119. New York: Wiley
126. Thompson K, Booske JH, Larson DJ, Kelly TF. 2005. Three-dimensional atom mapping of dopants in Si nanostructures. *Appl. Phys. Lett*. 87:052108/1–3
127. Kalinin SV, Bonnell DA. 2001. Electrostatic and magnetic force microscopy. In *Scanning Probe Microscopy and Spectroscopy*, ed. DA Bonnell, pp. 205–52. New York: Wiley
128. Sudbrack CK, Yoon KE, Noebe RD, Seidman DN. 2004. The temporal evolution of the nanostructure of a model Ni-Al-Cr alloy. *TMS Lett*. 1(2):25–26
129. Yoon KE, Noebe RD, Seidman DN. 2004. The role of rhenium on the temporal evolution of the nanostructure of a model Ni-Al-Cr superalloy. *TMS Lett*. 1(2):27–28

121. First APT chemical analysis of a semiconducting nanowire determining partitioning of solute atoms between the wire and catalyst.

Annual Review of
Materials Research

Volume 37, 2007

Contents

MATERIALS CHARACTERIZATION